

U-PB DATING AND GEOCHEMICAL CONSTRAINTS TO EARLY CRETACEOUS HYDROTHERMAL DOLOMITIZATION IN THE PROVENÇAL DOMAIN (MARITIME ALPS, NW ITALY - SE FRANCE)

Luca Barale*, Carlo Bertok**,✉, Anna d'Atri***, Fabrizio Piana*, Stefano M. Bernasconi***, György Czuppon°, László Palcsu°, Axel Gerdes°, Daniel Birgel* and Luca Martire**

* National Research Council of Italy, Institute of Geosciences and Earth Resources, Torino, Italy.

** University of Torino, Department of Earth Sciences, Torino, Italy.

*** ETH Zurich, Department of Earth Sciences, Zurich, Switzerland.

° Institute for Geological and Geochemical Research, Research Centre for Astronomy and Earth Sciences, Eötvös Loránd Research Network, Budapest, Hungary.

°° Isotope Climatology and Environmental Research Centre (ICER), Institute for Nuclear Research, Debrecen, Hungary.

°°° Goethe University Frankfurt, Department of Geosciences, Frankfurt am Main, Germany.

• University of Hamburg, Department of Earth Sciences, Institute for Geology, Hamburg, Germany.

✉ Corresponding author, e-mail: carlo.bertok@unito.it

Keywords: hydrothermal dolomitization; U-Pb carbonate datings; Early Cretaceous; Provençal Domain; Maritime Alps.

ABSTRACT

In the Maritime Alps (NW Italy - SE France), the Middle Triassic-Berriasian platform carbonates of the Provençal Domain are locally affected by an intense hydrothermal dolomitization. This dolomitization resulted from a large-scale hydrothermal circulation related to deep-rooted faults, and is indirect evidence of a significant earliest Cretaceous fault activity in this part of the Alpine Tethys European palaeomargin. New carbonate U-Pb dating and geochemical (stable isotope and noble gases on inclusion-hosted water, $^{87}\text{Sr}/^{86}\text{Sr}$, clumped isotopes) data allowed a better understanding of the timing and mechanisms of the hydrothermal circulation. Hydrothermal fluids probably originated from seawater, which was involved in a deep circulation within the underlying crystalline basement, undergoing heating to more than 200°C and substantial compositional modification by prolonged interaction with basement rocks. Thin cement rims rich in carbonaceous material, locally alternated with hydrothermal dolomite cements, are interpreted as remnants of ephemeral microbial communities that could colonize the upper part of hydrothermal conduits during periods of reduced hot fluid flow and contemporaneous downward seawater infiltration.

INTRODUCTION

The recognition of hydrothermal dolomitization can be crucial for the reconstruction of the tectono-stratigraphic and diagenetic evolution of carbonate successions currently exposed in orogenic chains, as it documents important fluid circulation related to extensional or transtensional tectonics, whose physical evidence such as main features could have been overprinted by younger compressive tectonics (e.g., Barale et al., 2016b; Incerpi et al., 2017; Mozafari et al., 2019). Hydrothermal dolomitization has significantly been overlooked in the past although it has been recognized that many cases of pervasive dolomitization, even at a regional scale, could be related to hydrothermal events (e.g., Davies and Smith, 2006; Luczaj, 2006). In the last 15 years, many hydrothermal dolomitization case studies have been described worldwide in the literature (e.g., Benjakul et al., 2020, and references therein). However, providing definitive evidence for a hydrothermal origin of dolomite is not always possible. It requires documenting that the temperature of fluid from which the dolomite formed was higher than the surrounding host carbonate rocks (Machel and Lonnee, 2002; Davies and Smith, 2006). This implies knowledge of the fluid temperature, and robust and independent constraints on the timing of dolomitization and related burial depth. Reliable estimation of the fluid temperature is routinely achieved using microthermometric analyses of primary fluid inclusions in dolomite crystals; recently, also clumped isotope geothermometry has been successfully applied to hydrothermal dolomites

(e.g., Ferry et al., 2011; Honlet et al., 2018; Koeshidayatullah et al., 2020). Direct, radiometric dating of hydrothermal dolomitization events is difficult, due to the typical absence of target-minerals coeval to dolomite suitable for radiometric dating; only recently, the development of U-Pb carbonate dating has allowed radiometric ages to be obtained on hydrothermal dolomites (Salih et al., 2019; Incerpi et al., 2020a; 2020b). In rare favourable cases, stratigraphic constraints such as the presence of dolomitized clasts in sediments slightly younger than the dolomitized successions allow a quite precise, though indirect, dating of hydrothermal dolomitization (e.g., Wilkinson, 2003; Barale et al., 2013; Shelton et al., 2019). More commonly, however, the age and hydrothermal nature of dolomitization are inferred on the basis of correlations with regional tectono-stratigraphic events (e.g., Lavoie and Morin, 2004; López-Horgue et al., 2010; Swennen et al., 2012; Hendry et al., 2015), or spatial association with faults of known displacement age (Hollis et al., 2017). Because of the uncertainty on the age, however, in all such cases little or no information on the depth of dolomite formation is provided, and even the hydrothermal rather than deep burial origin of dolomite remains questionable.

Another crucial point in the analyses of hydrothermal dolomite is related to the composition, origin and evolution of the dolimitizing fluids, which is fundamental for the reconstruction of the geometry of fossil hydrothermal systems. The main obstacle is represented by the difficulties to directly analyze the parent fluids. Combining homogenization temperatures of fluid inclusions with the oxygen isotope of dolo-

mite is a quite common indirect method to infer the original $\delta^{18}\text{O}$ of fluids, while the freezing behaviour of fluid inclusions can provide information on salinity and composition (e.g., Middleton et al., 1993; Boni et al., 2000; López-Horgue et al., 2010; Haeri-Ardakani et al., 2013; Hendry et al., 2015; Barale et al., 2016b). The main limitation is often a lack of primary fluid inclusions large enough to perform microthermometry in saddle dolomite due to its high precipitation rate.

The studied hydrothermal dolostones (Barale et al., 2016b) crop out in the Dauphinois-Provençal Domain, which has always been considered the proximal portion of the European continental margin (e.g., Debelmas and Lemoine, 1970; Debelmas and Kerckhove, 1980; Stampfli and Marthaler, 1990), originated during the Late Triassic-Early Jurassic by the Alpine Tethys rifting. The recognition of an Early Cretaceous hydrothermal dolomitization in the Provençal Domain provides a robust, although indirect, evidence of Early Cretaceous, post-rift tectonics in this sector of the European palaeomargin. The inferred temperature of the hydrothermal fluids and the large volumes of the rock bodies affected by dolomitization point to a huge and deep hydrothermal system, in turn related to deep-rooted faults (Barale et al., 2016b).

In the M. Marguareis area (External Ligurian Briançonnais), a few kilometres east of the study area, Bertok et al. (2012) documented the occurrence of kilometre-long Cre-

taceous palaeofaults, whose activity started during the Aptian and kept on in the Late Cretaceous. The presently N-S striking normal faults, which accommodated vertical displacements of several hundred metres, were confined by and kinematically related to two main transcurent zones, presently striking E-W. Bertok et al. (2012) suggested that such a setting could be consistent with a location of the External Ligurian Briançonnais at the easternmost end of a regional transform system, which has been inferred (e.g., Stampfli, 1993; Stampfli et al., 2002; Stampfli and Borel, 2002; Rosenbaum and Lister, 2005; Handy et al., 2010) to connect the Bay of Biscay to the Valais and Liguria-Piemonte oceans, at the Early-Late Cretaceous boundary. Tavani et al. (2018) proposed a refined geodynamic model where the Marguareis Cretaceous palaeofaults are interpreted as part of a crustal-scale extensional system located at the easternmost termination of the Iberia-Eurasia plate boundary, bounded by major NNE-SSW sinistral transfer faults.

Here we describe the results of a new set of analyses performed on samples from the hydrothermal dolomite bodies occurring in the Triassic-Jurassic succession of the Provençal Domain, Maritime Alps (Barale et al., 2016b; Figs. 1, 2).

In situ, U-Pb dating by laser ablation-inductively coupled plasma-mass spectrometry (LA-ICP-MS) was performed on the studied hydrothermal dolomites. U-Pb dating of carbon-

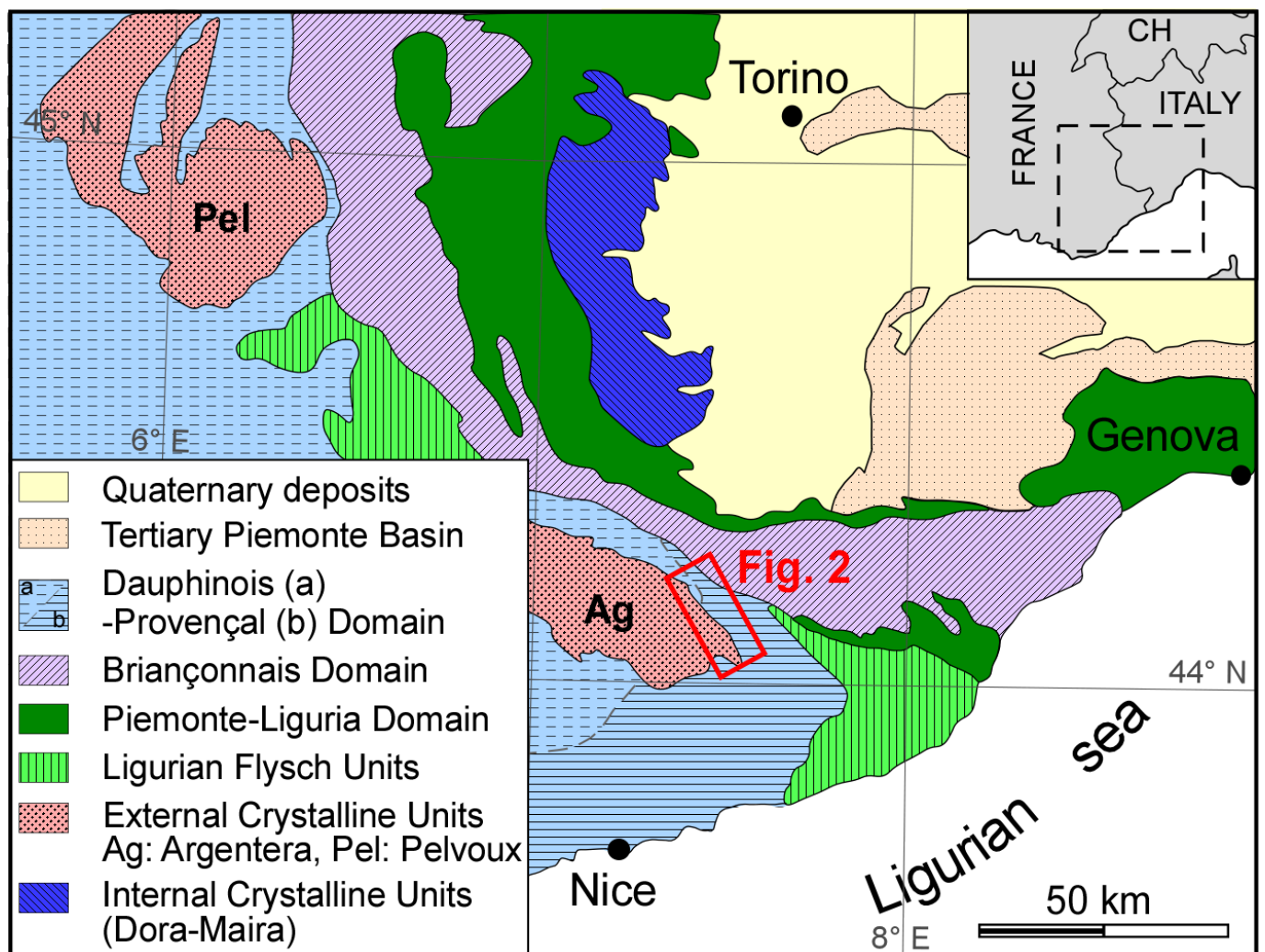


Fig. 1 - Schematic geographical and geological map of the SW Alps (from Barale, 2016b) with indication of the study area in Fig. 2.

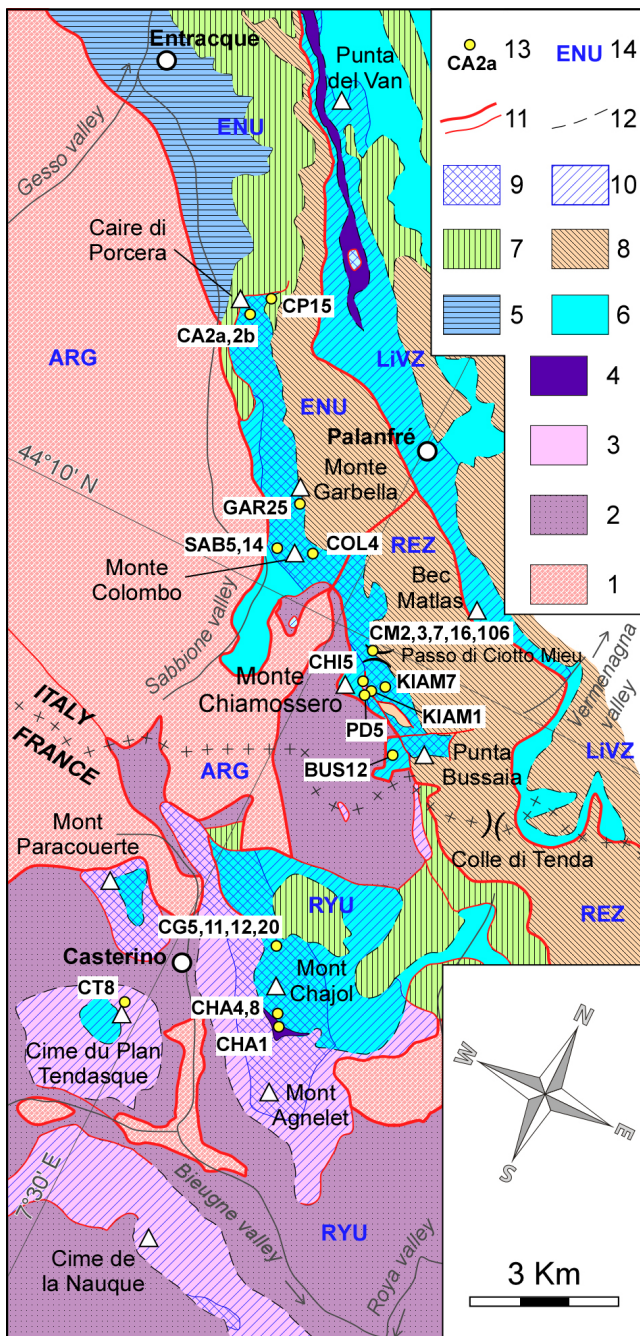


Fig. 2 - Geological scheme of the study area, showing the dolomitization degree of Middle Triassic-Jurassic carbonates, and the localization of the analyzed samples. 1- Argentera Massif crystalline basement. 2- Permian-Early Triassic siliciclastic deposits. 3- Middle Triassic carbonates. 4- Late Triassic-Early Jurassic succession. 5- Jurassic Dauphinois hemipelagic succession. 6- Middle Jurassic-Berriasian Provençal carbonates (Garbella Limestone). 7- Cretaceous succession. 8- Alpine Foreland Basin succession. 9- Intense hydrothermal dolomitization (local complete dolomitization of the host rock; common dolomite vein frameworks and dolomite-cemented breccias). 10- Moderate hydrothermal dolomitization (partial dolomitization of the host rock; rare dolomite vein networks and dolomite-cemented breccias). 11- Tectonic contacts (thick lines, first-order tectonic contacts separating tectonic units; thin lines, second-order tectonic contacts). 12- Stratigraphic contacts. 13- Sampling points. 14- Tectonic units (ENU, Ennacque Unit; RYU, Upper Roya Unit; ARG, Argentera Crystalline Massif) and deformation zones (LiVZ, Limone-Viozene Zone; REZ, Refrey Zone). Modified from: Barale et al., (2016a) (Italian part); Faure-Muret et al. (1967), Lanteaume (1990), and Malaroda (1999) (French part).

ates is a relatively new technique and is gaining increasing importance in studies dealing with primary (biogenic or not) and diagenetic calcite and aragonite precipitation (e.g., Denniston et al., 2008; Li et al., 2014; Godeau et al., 2018; Woodhead and Petrus, 2019; Kylander-Clark, 2020). Calcite U-Pb geochronology has also been widely used to constrain fluid circulation along faults and fractures at shallow crustal levels (e.g., Roberts and Walker, 2016; Hansman et al., 2018; Parrish et al., 2018; Salomon et al., 2020). On the other hand, U-Pb dating of dolomite is more challenging (Elisha et al., 2020); only recently, this technique was applied to high-temperature, fault- and fracture-related hydrothermal dolomite (Salih et al., 2019; Incerpi et al., 2020a; 2020b). The new U-Pb radiometric ages on dolomite presented here offer the double possibility to test the reliability of the U-Pb radiometric carbonate datings and confirm the timing of dolomitization inferred by Barale et al. (2016b) on the basis of stratigraphic constraints.

Additionally, stable isotope analyses of inclusion-hosted water, noble gases analyses, Sr isotopes measurements, and clumped isotope analyses were performed to obtain better constraints to the origin, the circulation pathways, and the temperature of the hydrothermal fluids.

GEOLOGICAL SETTING

The study area is located in the Maritime Alps (North-Western Italy) and extends for some tens of square kilometres between the Gesso valley to the North and the upper Roya valley to the South (Figs. 1, 2). This sector of the Western Alps comprises several tectonic units juxtaposed by NW-SE striking, mainly steeply dipping, Alpine tectonic contacts. These units constitute the southern part of a double vergent structure developed at regional scale (Gidon, 1972; Michard et al., 2004) that involves the Briançonnais Domain in the internal, north-eastern side, and the Dauphinois-Provençal Domain in the external, southwestern one (Carraro et al., 1970; d'Atri et al., 2016). More in detail, the Briançonnais domain is subdivided into an internal sector (Internal Briançonnais) affected by HP-LT metamorphism (Michard et al., 2004), and an external sector (External Briançonnais) affected by low-grade metamorphism (Piana et al., 2009; 2014). The Dauphinois-Provençal Domain is bounded, along its inner side, by the External Briançonnais Front; starting from the Jurassic, it differentiated into a basinal area, where a several km-thick and clay-rich succession was deposited (Dauphinois succession), and a shallow water one, which is characterized by a reduced thickness and carbonate platform facies (Provençal succession).

The current geological setting of the Briançonnais and Dauphinois-Provençal domains of the Maritime Alps is the result of the progressive involvement of the Palaeo-European continental margin, which these domains belong to, in the Alpine tectonic belt since the Middle Eocene (e.g., Dumont et al., 2012). The first stages of this tectonic evolution caused the development of a regional unconformity on top of the Mesozoic succession, corresponding to a hiatus spanning the latest Cretaceous-Middle Eocene. This is overlain by the Alpine Foreland Basin succession (Sinclair, 1997). Since the latest Eocene the continental margin and the foreland basin successions experienced a multistage tectonic evolution characterized by southward brittle-ductile thrusting and superposed foldings, followed by north-eastward back-vergent folding and southward brittle thrusting and flexural folding (d'Atri et al., 2016). The regional structural setting resulted from a transpressional regime (Piana et al., 2009; Molli et al., 2010; d'Atri et al., 2016),

documented by a post-Early Oligocene NW-SE transcurrent shear zone (Limone-Viozene Zone) extending for some tens kilometres through the study area. This shear zone is probably superimposed on a long-lived shearing corridor, active since the Jurassic-Cretaceous and reactivated during the Cenozoic (Bertok et al., 2012; d'Atri et al., 2016).

Although the Alpine deformation largely hinders the direct recognition of ancient structures, remnants of Cretaceous tectonic features (palaeofaults and related fluid circulation) have been locally documented on the basis of stratigraphic, geochemical, and structural data (e.g., Bertok et al., 2012; Barale et al. 2013; 2016b; Tavani et al., 2018).

The studied dolomitized rocks crop out in the Roaschia, Entracque and Roya tectonic units; the Refrey Zone and the Limone-Viozene Zone (d'Atri et al., 2016; Fig. 2). They are affected by very low-grade metamorphism which did not significantly modify the primary texture and mineralogical composition of the rocks. The Mesozoic successions of these units can be referred mostly to the (present-day) northern part of the Provençal platform, close to the transition to the Dauphinois basin (Carraro et al., 1970; Lanteaume, 1990; Barale et al., 2016a; 2017; d'Atri et al., 2016), which is represented only in the northern part of the Entracque Unit. The samples analyzed for this study come from the Middle Triassic-Jurassic succession of the Entracque Unit, upper Roya Unit, and Refrey Zone (see Table S1 for further information).

The Provençal succession starts with Permian continental sediments, locally up to 3000 to 4000 m thick, resting on the crystalline basement of the Argentera Massif (Faure-Muret, 1955). They are followed by some tens of metres of Early Triassic coastal siliciclastic deposits, Middle Triassic peritidal carbonates, and Late Triassic pelites and evaporites. The Middle Triassic carbonates are represented by a 150 to 200 m thick succession of limestones, dolomitic limestones, and fine-grained dolostones, with decimetre-thick bedding (Bersezio and d'Atri, 1986; Malaroda, 1999). Dark-coloured, organic-rich limestones and dolostones, a few tens of metres thick, are locally present above the Middle Triassic carbonates (Mont Chajol) and are attributed to the Late Triassic (Malaroda, 1999). The Late Triassic-Early Jurassic succession consists of a few tens of metres of continental reddish pelites and peritidal to open marine shelf carbonates (Barale et al., 2016a). These are followed by 200 to 300 m of Middle Jurassic-Berriasian platform limestones (Garbella Limestone; Barale, 2014; Barale et al., 2016a; 2017). They are overlain by an Early Cretaceous condensed succession, at most some tens of metres thick, consisting of bioclastic limestones and marly limestones, locally rich in authigenic minerals, followed by Late Cretaceous hemipelagic deposits (Lanteaume, 1968; Malaroda, 1999; Barale et al., 2017). The Mesozoic succession is overlain by the Alpine Foreland Basin succession (Sinclair, 1997), consisting of Middle Eocene discontinuous continental to lagoonal deposits (*Microcodium* Formation), Middle Eocene mixed carbonate-siliciclastic ramp deposits (Nummulitic Limestone), followed by Late Eocene hemipelagic sediments (*Globigerina* Marl) and the Late Eocene-Early Oligocene Grès d'Annot turbidite succession.

THE PROVENÇAL HYDROTHERMAL DOLOMITES

Hydrothermal dolomitization affects the Provençal carbonate succession, from the Middle Triassic carbonates to the Middle Jurassic-Berriasian shallow-water Garbella Limestone (Fig. 3; see also Fig. 3 in Barale et al., 2016b). The main char-

acters of this hydrothermal dolomitization system, fully described in Barale et al. (2013; 2016b), are briefly summarized below. Dolomitized bodies are irregularly shaped and vary in size from a few to hundreds of metres (Fig. 3a). Partially dolomitized limestones constitute the greatest volume of the dolomitized rocks in the study area, and show both selective (either matrix- or grain-selective) and non selective dolomitization fabrics. Entirely dolomitized rocks occur mainly in the Jurassic succession as metre-sized bodies, randomly distributed within partially dolomitized limestones, and are represented by fine to medium crystalline dolostones and white, sucrosic, coarse to very coarse crystalline dolostones.

Dolomitized bodies are commonly associated with networks of dolomite-cemented veins, showing no preferential orientation. Veins are 200 μm to 2 mm thick and consist of a thin inner part (100-200 μm), composed of fine to medium crystalline turbid dolomite and a thicker outer rim (100-1000 μm) composed of outward growing, coarse crystalline dolomite crystals (Fig. 3b).

Dolomite-cemented breccias are also commonly observed within the dolomitized rocks; they form tabular bodies, a few centimetres to some metres wide and up to some tens of metres long, which generally cross-cut bedding at a high angle. Breccias consist of mm- to cm-sized, angular to sub-rounded clasts, mainly of the same lithology as the encasing rock, showing a jigsaw puzzle arrangement and cemented by coarse crystalline dolomite (Fig. 3c). Irregularly shaped dissolution cavities, up to some decimetres in diameter, are frequent in the dolomitized rocks. Cavities are commonly fringed by a rim of coarse crystalline dolomite cement, followed by sparry calcite (Fig. 3d); laminated, fine-grained internal sediments of carbonate composition are also commonly observed plugging these cavities.

Replacement dolomite is mainly represented by fine to medium crystalline planar-s dolomite, with a turbid appearance in thin section (Dol1 of Barale et al., 2016b; Fig. 3e). Locally, in the micritic facies of the Garbella Limestone, euhedral, coarse to very coarse crystalline planar-e replacement dolomite crystals, up to 1-2 mm in size occur (Dol 2 of Barale et al., 2016b; Fig. 3e). Non-planar, coarse to extremely coarse crystalline (500-5000 μm) saddle dolomite (Dol 3 of Barale et al., 2016b; Fig. 3f, g), forms the widespread cements of veins, breccias and cavities, and also occurs as replacive dolomite in some sucrosic dolostones. Uniquely in a very limited sector (Mont Chajol area, see Fig. 2), in addition to Dol3, a fibrous dolomite cement (Dol4 of Barale et al., 2016b) occurs within breccias, cavities and fractures in the Late Triassic dolostones or at the base of the Garbella Limestone. It forms elongated, blade- to fan-shaped crystals with rhombic terminations, up to 7-8 mm long and 1-2 mm wide, and shows sweeping extinction with diverging optical axes of the fibres (fascicular-optic).

The last phase of void filling, ubiquitously postdating dolomite cements in the whole study area, is a coarsely to extremely coarsely crystalline sparry calcite (Cc1), generally limpid in thin section, showing a white to locally dark-grey or blackish colour on the hand sample.

Field and petrographic observations indicate that dolomitization was a polyphase process, in which episodes of hydrofracturing and host-rock dissolution, related to expulsion of overpressured fluids through faults and fracture systems, were associated with phases of host-rock dolomitization and void cementation. The presence of clasts of dolomitized rocks in sediments slightly younger than the youngest dolomitized rocks, allowed precise dating of the dolomitization event (latest Berriasian-Valanginian interval). This, in turn, allowed a direct evaluation of the burial setting of dolomitiza-

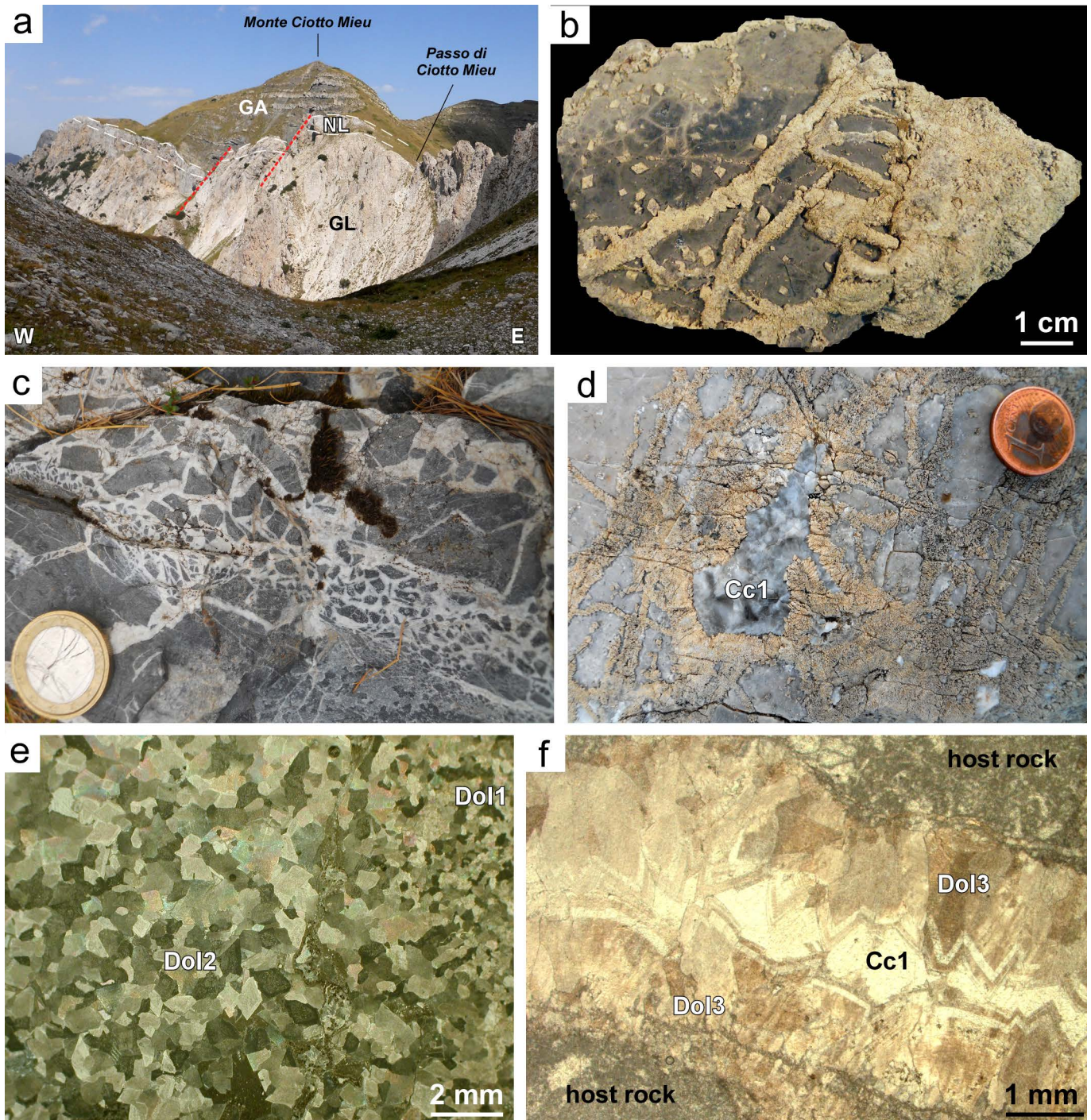


Fig. 3 - a) Western side of Passo di Ciotto Mieu: cliff of dolomitized Garbella Limestone (GL, about 100 m high) unconformably overlain by the Alpine Foreland Basin succession (Nummulitic Limestone and *Globigerina* Marl, NL; Grès d'Annot, GA). Image taken from the eastern side of Monte Chiamossero (44°09'39.0"N, 7°30'45.2"E). b) Hand sample of Garbella Limestone showing different degrees of dolomitization. The left portion is only partly dolomitized with scattered euhedral crystals of dolomite; the right portion is fully dolomitized, whereas in the middle portion dolomitization follows a network of veins. c) Breccia in Middle Triassic carbonates, made up of centimetre-sized, angular clasts cemented by withish, coarse crystalline dolomite (Mont Agnelet). d) Cm-sized dissolution cavity in a portion of Garbella Limestone rich in dolomite veins. The cavity is rimmed by coarse crystalline dolomite cement and plugged by grey-coloured sparry calcite (Cc1). Passo di Ciotto Mieu. e) Thin section photomicrograph (crossed polars) of dolomitized Garbella Limestone showing transition from medium crystalline planar-s Dol1 to coarse crystalline planar-e Dol2. Punta Bussaia. f) Thin section photomicrograph (plane light) of a cavity within undolomitized Garbella Limestone, rimmed by coarse crystalline, zoned Dol3 and plugged by Cc1 sparry calcite. Sabbione Valley.

tion, which occurred when the Provençal carbonates were at a very shallow burial depth (from a few tens of metres for the uppermost, Berriasian, part of the succession to about 500 m for the lowermost, Triassic part).

Homogenization temperatures of primary fluid inclusions

in dolomite cements indicate that dolomitizing fluids were relatively hot (170-260°C); final melting temperatures point to highly saline fluids with a complex composition that could be represented by the NaCl-CaCl₂-MgCl₂-H₂O system and an approximate salinity of 20-23% CaCl₂ equivalent.

The isotopic composition of hydrothermal dolomites shows slightly positive $\delta^{13}\text{C}$ values and negative $\delta^{18}\text{O}$ values varying from -2 to -11‰ VPDB. The latter, combined with precipitation temperature obtained by fluid inclusion microthermometry, indicate highly ^{18}O -enriched parent fluids (+9 to +12‰ VSMOW; Barale et al., 2016b, calculated with the fractionation equation of Land, 1985). Re-calculation of parent fluid composition using the same data and the newer fractionation equation of Müller et al. (2019) indicates a composition ranging between +11.2 and +14.9‰ VSMOW.

The high temperature of the fluids, which contrasts with the inferred shallow burial setting, points to a very deep hydrothermal circulation related to deep-rooted fault systems. This deep circulation indisputably involved the Permian-Early Triassic siliciclastic rocks and the crystalline basement rocks of the Argentera Massif, due to the modest thickness of the Mesozoic succession (about 500-600 metres). Interaction with siliciclastic and basement rocks could also account for the inferred composition of the dolomitizing fluids. In fact, based on the regional geological setting, Barale et al. (2016b) concluded that the most likely source for hydrothermal fluids was seawater, whose original composition had to be strongly modified to produce highly saline, ^{18}O -enriched dolomitizing brines.

ANALYTICAL METHODS

Cathodoluminescence, SEM-EDS, micro-Raman spectroscopy

CL observations were carried out on polished thin sections using CITL 8200 mk3 equipment (operating conditions of ca 17 kV and 400 μA). In situ quantitative microprobe analyses were performed on carbon-coated thin sections with an energy dispersive X-ray spectroscopy (EDS) Energy 200 system and a Pentafet detector (Oxford Instruments) associated with a Cambridge Stereoscan S-360 scanning electron microscope (SEM). The operating conditions were 15 kV of accelerating voltage, ca 1 nA of probe current, and 50 sec of counting time. The SEM-EDS quantitative data (spot size: 2 μm) were acquired and processed using the Microanalysis Suite Issue 12, INCA Suite version 4.01; Structure Probe, Inc. natural mineral standards were used to calibrate the raw data; the RoPhiZeta correction (Pouchou and Pichoir, 1988) was applied. Analytical statistical errors R on atomic weight per cent are 008 for Mg and Fe and 013 for Ca. Micro-Raman spectroscopy was performed with a LabRAM-HR 800 (HORIBA - JOBIN-YVON) spectrometer using a HeNe laser (633 nm, 20 mW). These analyses were carried out at the Department of Earth Sciences, University of Torino.

Lipid biomarkers

Sample CG 11 was chosen for the analyses of lipid biomarkers. Prior to extraction, the sample was cut to avoid contamination. Then 85 g of sample were crushed to small pieces and decalcified by pouring slowly 10% HCl onto the sample, after the method described by Birgel et al. (2006). The residual material was saponified with 6% KOH in methanol. The saponification extract was collected, then the sample was extracted three times with a CEM microwave extraction system at 80°C at 250W for 15 minutes with a mixture of dichloromethane + methanol (3+1). The saponification extract was combined with the three other extracts. Then, the mixture was acidified with 10% HCl to release the fatty acids

from the aqueous phase and cleaned with water in a separatory funnel. The organic extract was collected and reduced by rotary evaporation. The reduced total lipid extract was then pre-cleaned by separation into a *n*-hexane soluble maltene and dichloromethane soluble asphaltene fraction. For GC analyses, the maltene fraction was further separated by solid-phase column chromatography into four fractions of increasing polarity as mentioned in Birgel et al. (2008a). All four fractions were measured by gas chromatography-flame ionization detection (GC-FID) with an Agilent 7820 A GC system at the University of Vienna. The GC was equipped with a 30 m HP-5 MS UI fused silica capillary column (0.25 mm i.d., 0.25 mm film thickness). The carrier gas used was helium. The GC temperature program used was: 60°C (1 min) from 60°C to 150°C at 8°C/min, then to 320°C at 4°C/min. Then 25 minutes isothermal. After GC-FID analyses of all four fractions, only the hydrocarbon fraction contained some minor compounds. Only the hydrocarbon fraction was also measured by an Agilent 7890 A GC system coupled to an Agilent 5975C mass spectrometer, to identify the individual compounds. The GC-conditions were identical to those described for the GC-FID measurements.

Sr isotopes

$^{87}\text{Sr}/^{86}\text{Sr}$ ratios for samples CG12, CHA4, CM3, and COL4 were measured with a Finnigan MAT 262V multi-collector mass spectrometer at the CNR, Institute of Geosciences and Earth Resources of Pisa (Italy), running in dynamic mode. Conventional ion exchange methods were used for Sr separation from the matrix. Measured $^{87}\text{Sr}/^{86}\text{Sr}$ ratios were normalized to $^{86}\text{Sr}/^{88}\text{Sr} = 0.1194$. During the collection of isotopic data replicate measurements of NIST SRM 987 (SrCO_3) standard yielded values of 0.710242 ± 17 (2 s, N = 19). $^{87}\text{Sr}/^{86}\text{Sr}$ ratios for samples CHA1, CHI5 and SAB5 were measured in situ at the Goethe University Frankfurt (Germany), using a Thermo-Finnigan Neptune multi-collector inductively coupled plasma - mass spectrometer (MC-ICP-MS) attached to a RESOLUTION 193 nm Ar-F Excimer laser ablation system (ComPexPro 102F, Coherent), equipped with an S-155 two-volume (Laurin Technic, Australia) ablation cell. Laser spots with diameters of 120-235 μm were drilled with a repetition rate of 8 Hz, and energy density of about 6-7 J/cm², during 45 s of data acquisition. The depth penetration of the static spots was about 0.7 $\mu\text{m s}^{-1}$. Ablation and material transport occurred in a sample gas stream of Ar (0.8 l min⁻¹) mixed with He (0.6 l min⁻¹) and N₂ (0.005 l min⁻¹), and signal homogenization directly after ablation was carried out using a "Squid" (Laurin Technic, Australia). Wash out time for all important isotopes was less than 5 seconds, which allowed a relatively high sample throughput of ca. 20-30 measurements per hour. The raw data of $^{86}\text{Sr}/^{87}\text{Sr}$ were corrected for blank (mostly ^{84}Kr , ^{86}Kr in sample gas), and isobaric interferences arising from double-charged rare earth elements (Er, Yb), as well as for Ca dimers and Rb. Corrections for Kr, Er, Yb had only a negligible effect due to extremely low intensities for ^{167}Er , ^{173}Yb (< 0.0001 Volt), and ^{83}Kr (< 0.0007 Volt). In contrast, Rb interference correction was important. At the beginning of the analytical session, soda-lime glass SRM-NIST 610 was measured 2-3 times for empirical determination of $^{87}\text{Rb}/^{85}\text{Rb}$ mass bias using the Sr mass bias ($^{86}\text{Sr}/^{88}\text{Sr}_m$ relative to $^{86}\text{Sr}/^{88}\text{Sr}_{true} = 0.1194$) of each integration multiplied by an off-set factor. The procedure yielded after successful interference correction on ^{86}Sr , ^{88}Sr , and ^{85}Rb from doubly charged Yb and Er the $^{87}\text{Rb}/^{86}\text{Sr}$ ratio needed

for accurate correction of the isobaric interference of ^{87}Rb on ^{87}Sr . Despite the high $^{87}\text{Rb}/^{86}\text{Sr}$ of 2.82, with an ^{87}Rb 4 times the ^{87}Sr , we obtained an $^{87}\text{Sr}/^{86}\text{Sr}$ (0.7096 ± 0.0010 ; $n = 12$), which is within the uncertainty of the reported value of Woodhead et al. (2001). Performance and accuracy were checked by multiple measurements of the feldspar in-house standard MIR-1, an isotopically homogeneous plagioclase megacryst from a lava of the Dutsin Miringa Hill volcano (Northern Cameroon Line; Rankenburg et al., 2004). The results of standard measurements yielded values of $^{87}\text{Sr}/^{86}\text{Sr}$, which were in agreement (within error) to conventional TIMS data of 0.703096 ± 0.000070 (2σ , Rankenburg et al., 2004).

δD , $\delta^{18}\text{O}$ and He-Ar isotopes of fluid inclusion-hosted waters

Stable hydrogen and oxygen isotope composition of the inclusion-hosted water and the water content of carbonate (dolomite and calcite) samples were determined at the Institute for Geological and Geochemical Research (Budapest, Hungary), using the laser spectrometric method described in detail by Czuppon et al. (2014) and Demény et al. (2016). The carbonate chips (1-4 gram) were crushed in a 10 mm OD stainless steel tube attached to the vacuum line and the liberated fluid, following trapping and cleaning procedure, was introduced to the laser spectroscope and measured. The hydrogen isotope composition is expressed as δD and $\delta^{18}\text{O}$ values (in ‰) relative to VSMOW (Coplen et al., 1996).

Helium and argon isotope composition of the inclusion-hosted water were determined at the Isotope Climatology and Environmental Research Centre (ICER; Debrecen, Hungary). About 1.0-2.0 g of sample material was placed in a stainless steel cylinder including an iron ball. After evacuating the system, the sample was crushed with the iron ball actuated manually by a magnet from outside. Most of the liberated gases were collected in an empty trap held at 25 K, while helium in a charcoal trap at 10 K. After heating the charcoal trap to 42 K, the helium was admitted to a VG5400 noble gas mass spectrometer. The argon fraction was released at 55 K, purified by a getter trap (SAES St 707), and then admitted to the same mass spectrometer. The measurement process was calibrated with well-known air aliquots in the range of $1 \cdot 10^{-3}$ to $1 \cdot 10^{-2}$ ccSTP (cubic centimetre at standard temperature and pressure) for helium and $2 \cdot 10^{-5}$ to $1 \cdot 10^{-4}$ ccSTP for argon.

Clumped C-O isotopes

The clumped isotope composition of dolomite and calcite was determined at the ETH Zurich using a Thermo Fisher Scientific 253Plus mass spectrometer coupled to a Kiel IV carbonate preparation device, following the method described in Meckler et al. (2014) and Müller et al. (2017). The Kiel IV device includes a custom-built Porapak Q trap held at -40°C to eliminate potential organic contaminants. Before each sample run, the pressure-dependent negative backgrounds are determined on all beams to correct for non-linearity effects. During each run, 18 replicates of 90-110 μg of different samples and 5 replicates of each of the three carbonate standards, ETH-1, ETH-2 and 8 replicates ETH-3 (Bernasconi et al., 2018), are analyzed for data normalization. Two replicates of the international standard IAEA C2 are analyzed to monitor the instrument long term reproducibility. All instrumental and data corrections are carried out with the software Easotope (John and Bowen, 2016) using the revised IUPAC parameters for ^{17}O correction (Bernasconi

et al., 2018). Clumped isotopes for dolomite are reported in the carbon dioxide equilibration scale (CDES) phosphoric acid reaction temperature of 70°C , whereas those of calcite are reported for a reaction temperature of 25°C . Temperature uncertainties are reported at the 95% confidence level (Fernandez et al., 2017; Bernasconi et al., 2018). D47-temperatures and isotopic composition of waters in equilibrium with the dolomite are calculated with the dolomite-specific calibrations of Müller et al. (2019). For calcite we used the calibration in Bernasconi et al. (2018). The composition of the fluids was calculated using the oxygen isotope calibration of O'Neil et al. (1969).

U-Pb dating

Uranium-Lead data were acquired in situ on polished thin sections from different samples by laser ablation-inductively coupled plasma-mass spectrometry (LA-ICP-MS) at the Goethe University Frankfurt (GUF), using a method modified by Gerdes and Zeh (2006; 2009). At GUF a Thermo Scientific Element 2 sector field ICP-MS is coupled to a Resolution S-155 (Resonetics) 193 nm ArF Excimer laser (CompexPro 102, Coherent) equipped with a two-volume ablation cell (Laurin Technic, Australia). Samples were ablated in a helium atmosphere (0.6 l/min) and mixed in the ablation funnel with 0.7 l/min argon and 0.04 l/min nitrogen. Signal strength at the ICP-MS was tuned for maximum sensitivity while keeping oxide formation below 0.3% (UO/U). Static ablation used a spot size of 213 μm and a fluence of $< 1 \text{ J cm}^{-2}$ at 6 Hz. This yielded SRM-NIST 614 a depth penetration of about 0.5 $\mu\text{m s}^{-1}$ and an average sensitivity of 420000 cps/ $\mu\text{g g}^{-1}$ for ^{238}U . The detection limits for ^{206}Pb and ^{238}U were ~ 0.1 and 0.03 ppb, respectively. However, at a U signal of less than 1000 cps (~ 2 ppb) the data were generally discarded due to enhanced scatter on the isotope ratios.

Each analysis consisted of 20 s background acquisition followed by 20 s of sample ablation and 25 s washout. During 42 s data acquisition, the signal of ^{206}Pb , ^{207}Pb , ^{208}Pb , ^{232}Th and ^{238}U were detected by peak jumping in pulse counting mode with a total integration time of 0.1 s, resulting in 420 mass scans. Before analysis each spot was pre-ablated for 3 s to remove surface contamination. Soda-lime glass SRM-NIST 614 was used as a reference glass together with two carbonate standards to bracket sample analysis.

Raw data were corrected offline using an in-house MS Excel© spreadsheet program (Gerdes and Zeh 2006; 2009). Following background correction, outliers ($\pm 2\sigma$, standard deviation) were rejected based on the time-resolved $^{207}\text{Pb}/^{206}\text{Pb}$ and $^{206}\text{Pb}/^{238}\text{U}$ ratios. The $^{207}\text{Pb}/^{206}\text{Pb}$ ratio was corrected for mass bias (0.3%) and the $^{206}\text{Pb}/^{238}\text{U}$ ratio for inter-element fraction (ca. 5%), including drift over the 12 hours of sequence time, using SRM-NIST 614. Due to the carbonate matrix an additional correction of 3% has been applied on the $^{206}\text{Pb}/^{238}\text{U}$, which was determined using WC-1 carbonate reference material dated by TIMS (254.4; Roberts et al., 2017). Thirty-four runs of the WC-1 carbonate standard over the course of the two analytical sessions provided a lower intercept age of $254.1 \pm 1.1 \text{ Ma}$ (2σ). Repeated analyses ($n = 35$) of a Zechstein dolomite ($255 \pm 4 \text{ Ma}$; Gypsum pit, Tettendorf, Germany) used as secondary (in-house) standard yielded a lower intercept age of $256.0 \pm 2.0 \text{ Ma}$ (MSWD: 1.3), implying an accuracy and repeatability of the method of around 2% or better. Data were plotted in the Tera-Wasserburg diagram, and ages calculated as lower intercepts using Isoplot 3.71 (Ludwig, 2009). All uncertainties are reported at the 2σ level.

RESULTS

The analyses of new samples and the application of other analytical techniques generally confirm the overall picture of the hydrothermal system described in Barale et al. (2016b) but provide new details on some aspects of its functioning.

Dolomite rims rich in carbonaceous material

Locally, in the Mont Chajol area (Fig. 2) a new type of dolomite cement (Dol5), which had not been previously described, was identified. It is a rim of pore-filling dolomite cement interposed in places between two different generations of Dol4 dolomite, in breccias, cavities and fractures in the Late Triassic dolostones or at the base of the Garbella Limestone. The rim is recognizable due to its black colour in hand sample (Fig. 4a, b), caused by the presence of carbonaceous material. Micro-Raman spectroscopy shows two broad bands at approximately 1330 cm^{-1} and 1610 cm^{-1} (see Fig. S2) which is strong evidence for organic matter. The rim is about one millimeter thick, and composed of two layers. The first is 100-200 μm thick and consists of a finely-crystalline, granular, dolomite, showing a moderate to dull red cathodoluminescence with a thin non-luminescent band (Fig. 4c-e). The reddish part is characterized by small (10-20 micron) bright, reddish patches. Aggregates of Fe-oxides are locally observed; they show a cubic habit, probably indicating their origin as pseudomorphs of pyrite crystals (Fig. 4b). The second layer is a radial-fibrous, mainly non-luminescent, dolomite with rhombic terminations, and shows a well-developed zonation defined by alternating limpid and turbid, brown-coloured, growth zones (Fig. 4c-e). SEM-EDS analyses show that Dol5 dolomite is non-ferroan, Ca-enriched dolomite, with a composition of around 40-42 mol% of MgCO_3 . U-Pb analyses on dolomite cements (see below) showed enrichment in U (up to 23 ppm) within this rim. Stable isotope analyses of this rim provided negative $\delta^{18}\text{O}$ values (-9.18, -8.94‰ VPDB) and slightly positive $\delta^{13}\text{C}$ values (+1.49, +1.28‰ VPDB). An analysis of the organic compounds by gas-chromatography has been carried out on Dol5. It showed a generally low content of organic compounds.

Black carbonaceous material (showing two broad bands at approximately 1330 cm^{-1} and 1610 cm^{-1} in micro-Raman spectroscopy; see Fig. S1) is also locally found as the infill of several-tens-of microns-thick fractures in the host rock (Fig. 4f) and as an impregnation of dispersed, fine particles within

the host rock, closely associated with fractures and forming several-mm-thick bands with a clear trend of increasing blackening towards the fracture walls (Fig. 4g).

Sr isotopes

Eight samples were measured for $^{87}\text{Sr}/^{86}\text{Sr}$ values (Fig. 5). Coarse crystalline dolomite cements (Dol3 saddle dolomite and Dol 4 fascicular-optic dolomite of Barale et al., 2016b), show values between 0.70778 ± 0.00008 and 0.710255 ± 0.000008 . Fine crystalline, replacement dolomite shows values between 0.70776 ± 0.00025 and 0.70900 ± 0.00047 . Finely crystalline, dolomitized internal sediments within dissolution cavities show values between 0.70879 ± 0.00017 and 0.71021 ± 0.00020 .

δD , $\delta^{18}\text{O}$ and He-Ar isotopes of fluid inclusions water

The hydrogen and oxygen isotope compositions (δD and $\delta^{18}\text{O}$) of the fluid inclusion water in the replacement dolomite range from -69 to -78‰ and from -2.6 to -1.3‰ respectively (Table 1). The δD and $\delta^{18}\text{O}$ values of the fluid inclusion water in dolomite cements are characterized by systematically higher values relative to replacement dolomite; the δD and $\delta^{18}\text{O}$ vary from -48 to -56‰ and 0.6 to 5.1‰, respectively (Table 1). The water content shows similar ranges for both types of dolomite, varying between 270 and 550 ppm. The stable isotope composition of fluid inclusions in calcite is very different from that of dolomite (Table 1). Both hydrogen and oxygen isotope composition ($\delta\text{D} = -93$ to -85 ‰; $\delta^{18}\text{O} = -14.0$ to -13.3 ‰) show higher negative values, and they plot close to the Global Meteoric Water Line (Fig. 6, GMWL: $\delta\text{D} = 8 \times \delta^{18}\text{O} + 10$, Dansgaard, 1964).

The measured helium and argon isotope composition of Dol3 and Dol4 cements is listed in Table 2. The helium isotope composition ($^3\text{He}/^4\text{He}$) is characterized by lower values than air (1Ra), ranging from 0.02 to 0.07 Ra. The argon isotope ratios ($^{40}\text{Ar}/^{36}\text{Ar}$) are systematically higher than air values (295.5), ranging from 340 to 520.

Clumped C-O isotopes

Clumped isotopes measurements were performed on a few samples of coarse crystalline dolomite cements (see Table S2). Three samples of coarse-crystalline Dol3 (CM3, Refrey Zone; CA2a-4 and SAB14b, Entracque Unit) gave

Table 1 - δD , $\delta^{18}\text{O}$ of fluid inclusions-hosted water in dolomite and calcite.

SAMPLE	phase	δD [‰, SMOW]	$\delta^{18}\text{O}$ [‰, SMOW]	H_2O concentration [ppm]
BUS 12	Replacement (Dol2)	-78.38	-1.26	352
CM2	Replacement (Dol1)	-69.03	-2.61	564
CM 16 dol	Replacement (Dol1)	-69.83	-1.28	494
CM 16 calc	Cc1 cement	-89.61	-14.05	209
SAB 14	Cc1 cement	-85.12	-13.61	103
KIAM 1 calc	Cc1 cement	-93.57	-13.30	594
PD 5	Dol3 cement	-49.71	5.14	482
KIAM 1 dol	Dol3 cement	-56.20	0.57	272
CG 5	Dol4 cement	-47.82	1.62	550

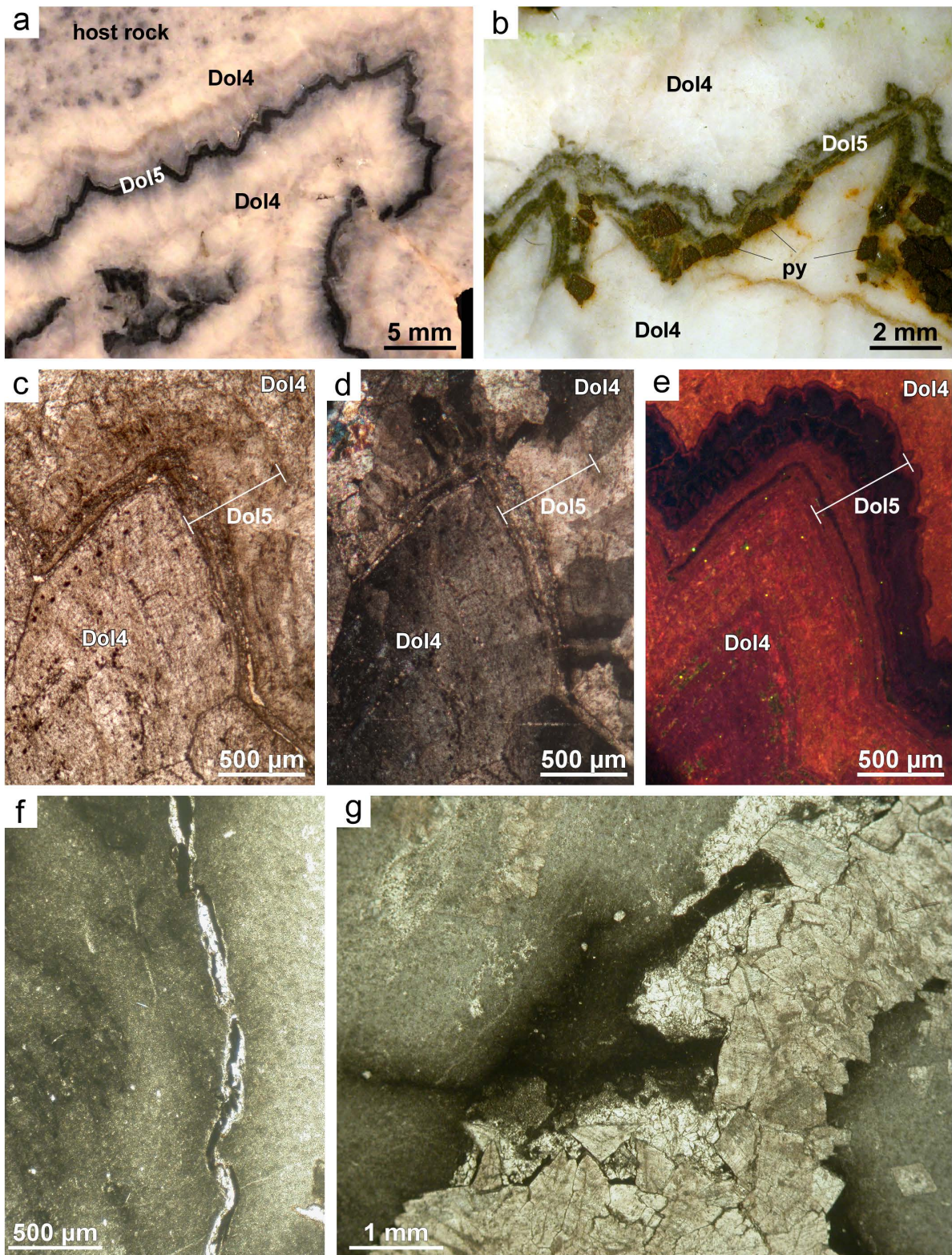


Fig. 4 - a-e) Dol5 rims (sample CG12, see location in Fig. 2). a) Polished surface showing black-coloured Dol5 rim interposed between two different generations of Dol4 cement. b) Polished surface showing a Dol5 rim, composed of a first, black-coloured layer with aggregates of Fe-oxides showing a cubic habit (py), probably indicating their origin as pseudomorphs on pyrite crystals, and a second layer composed by a white and a blackish band. c-e) Thin section photomicrograph (a, plane light; b, crossed polars; c, cathodoluminescence-CL) of a Dol5 rim, consisting of two layers. The first layer, 100-200 μm thick, is a finely-crystalline, granular, dolomite, showing a moderate to dull red CL with a thin non-luminescent band (the reddish part is characterized by the presence of small brighter, reddish patches). The second layer is a radial-fibrous, mainly non-luminescent in CL, dolomite with rhombic terminations, and shows a well-developed zonation defined by alternating limpid and turbid, brown-colored, growth zones. f) Thin section photomicrograph (plane light) showing a thin fracture in Garbella Limestone filled by black carbonaceous material. g) Thin section photomicrograph (plane light) showing an impregnation of dispersed, fine particles of carbonaceous material, closely associated with dolomite veins and forming several-mm-thick bands with a clear trend of increasing blackening towards vein walls.

For interpretation of the references to colour in this figure, the reader is referred to the online version of this paper.

Table 2 - Helium and argon isotope composition of Dol3 and Dol4 cements.

SAMPLE	Helium (ccSTP/g)	R/Ra	$^{40}\text{Ar}/^{36}\text{Ar}$
KIAM1 (Dol3 cement)	2.14E-07	0.03	397.6
KIAM7 (Dol3 cement)	1.13E-06	0.024	519.3
CT8 (Dol3 cement)	2.61E-06	0.037	340.1
CHA1 (Dol4 cement)	7.85E-07	0.067	345.6

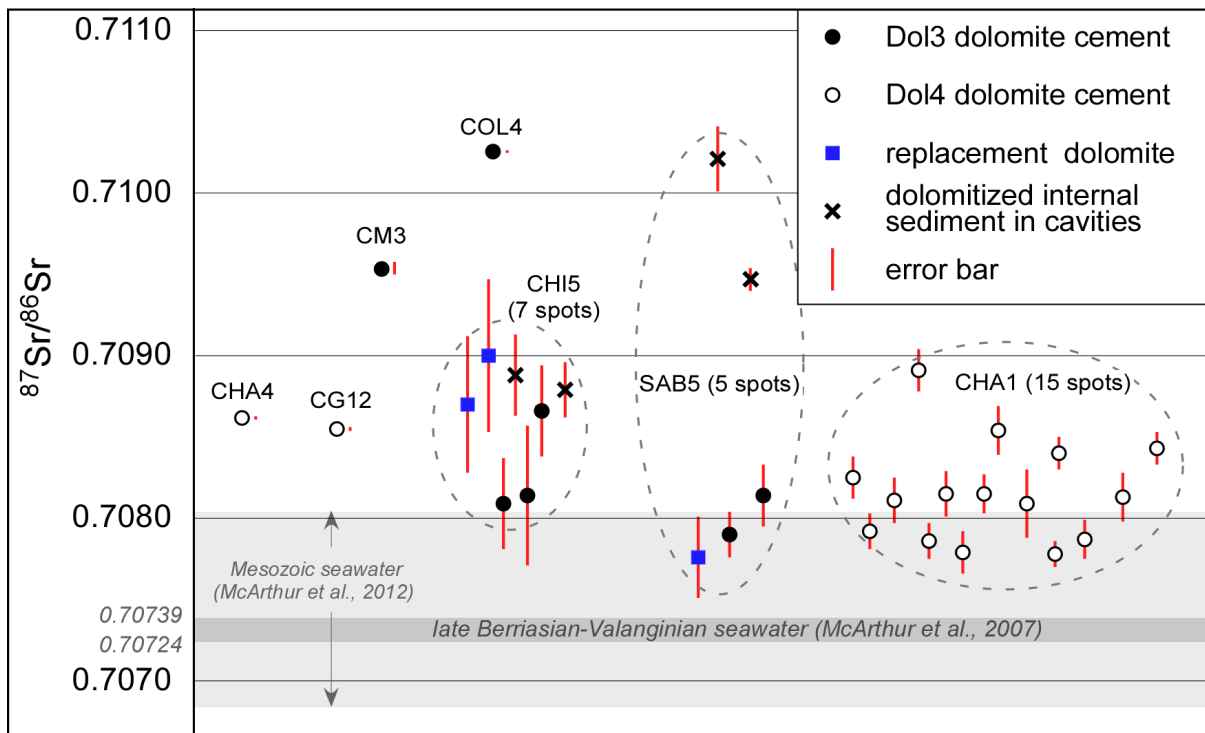


Fig. 5 - $^{87}\text{Sr}/^{86}\text{Sr}$ values measured on samples of Dol3 and Dol4 cements, replacement dolomite (Dol1), and dolomitized internal sediments of cavities (see sample position in Fig. 2). $^{87}\text{Sr}/^{86}\text{Sr}$ seawater values for Mesozoic (McArthur et al., 2012) and late Berriasian-Valanginian interval (McArthur et al., 2007) are shown for comparison.

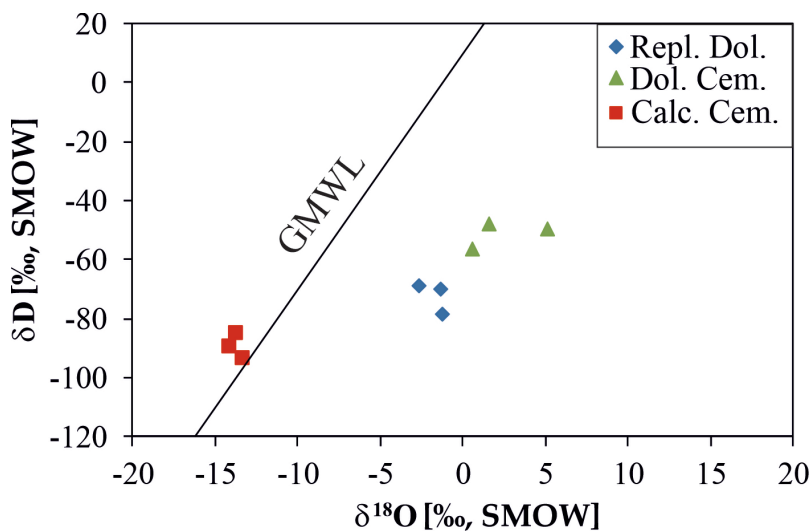


Fig. 6 - Measured hydrogen and oxygen isotope composition of inclusion-hosted water in dolomite and calcite. The global meteoric water line (GMWL, Dansgaard, 1964) is also shown.

$\Delta 47$ temperatures of 309°C, 258°C, and 351°C, respectively. One sample of coarse-crystalline Dol4 cement (CG12, Upper Roya Unit) gave a $\Delta 47$ temperature of 325 °C. Two Cc1 calcite samples (SAB 14a and CA2a-2, Entracque Unit) gave $\Delta 47$ temperatures of 270°C and 292°C, respectively.

U-Pb dating

In situ U-Pb isotope analyses were performed on different sites on 12 samples (see Fig. 2 and Table S1 for location). Five samples did not yield results due to very low uranium contents or too small variability of the U and Pb concentration and thus the limited spread in $^{238}\text{U}/^{206}\text{Pb}$ ratios. Uranium and Pb concentrations of the other 7 samples are variable and positively correlated, ranging from 0.01 to 23.3 ppm and from 0,02 to 27.9 ppm, respectively (see Table S3). Spot analyses commonly plot along a linear array in the $^{207}\text{Pb}/^{206}\text{Pb}$ vs. $^{238}\text{U}/^{206}\text{Pb}$ space (Tera-Wasserburg diagram, see Fig. S2). This array is interpreted as a mixture of initial common Pb and Pb formed due to in situ decay of U since dolomite crystallization. The age of formation is defined by the lower intercept with the Concordia. In Fig. 7 the age of each analyzed site is plotted with the respective 2σ error.

Sample CA2a is a slightly dolomitized bioclastic rudstone from the upper part of the Garbella Limestone. Three distinct sites were analyzed: site CA2a-1 (164±31 Ma) is an original micritized shell of a mollusc, site CA2a-2 (149±25 Ma) is an early diagenetic calcite cement rimming a gastropod shell, site CA2a-3 (125±47 Ma) is a calcite sparry cement replacing a gastropod shell. Sample CHI5 was collected from the Middle Triassic dolostones; two different sites were analyzed: site CHI5-1 (72.5±6.6 Ma) is a Dol3 cement rimming a cavity, site CHI5-2 (45.6±3.2 Ma) is a dolomitized in-

ternal sediment in the same cavity. Samples CM7, CM106, CHA8, SAB5 were collected from the dolomitized Garbella Limestone. On sample CM7 two distinct sites were analyzed: site CM7-1 (150±13 Ma) is a Dol3 cavity cement, site CM7-2 (129±36 Ma) is the sparry calcite cement plugging the same cavity. On sample CM106 two distinct sites were analyzed: site CM106-1 (133±16 Ma) is a replacive Dol3, site CM106-2 (123±14 Ma) is a Dol3 cement rimming a cavity. In the sample CHA8 the site CHA8-2 (47.66±0.24 Ma) is a black dolomite cement rim (Dol5) between two generations of Dol4 cements (site CHA8-1, 47.16±0.62 Ma, and site CHA8-3, 46.4±1.9 Ma, respectively). On sample SAB5 two distinct sites were analyzed: site SAB5-1 (57.9±1.3 Ma) is a replacive Dol3, site SAB5-2 (57.3±1.5 Ma) is a Dol3 void-filling cement. Sample CP15 is a lithoclastic floatstone with dolomitized clasts in the slope sediments covering the Caire Porcera palaeo-escarpment (Lausa Limestone; Barale et al., 2017): site CP15-1 (129±36 Ma) is a dolomitized clast, site CP15-2 (25±7 Ma) is the microsparitic matrix, site CP15-3 (22±11 Ma) is a thin calcite vein crossing both clasts and matrix.

INTERPRETATION

Dolomite rims rich in carbonaceous material

Dol5 dolomite, only found in the Mont Chajol area, forms a sharply-bounded, finely crystalline thin band, including abundant finely dispersed organic matter, interposed within coarsely-crystalline, limpid Dol4 dolomite. This records a short-lived event during which the growth of coarsely crystalline cements was inhibited and replaced by precipitation of a finely crystalline dolomite incorporating organic matter. The abundant organic matter within Dol5 dolomite rims can be

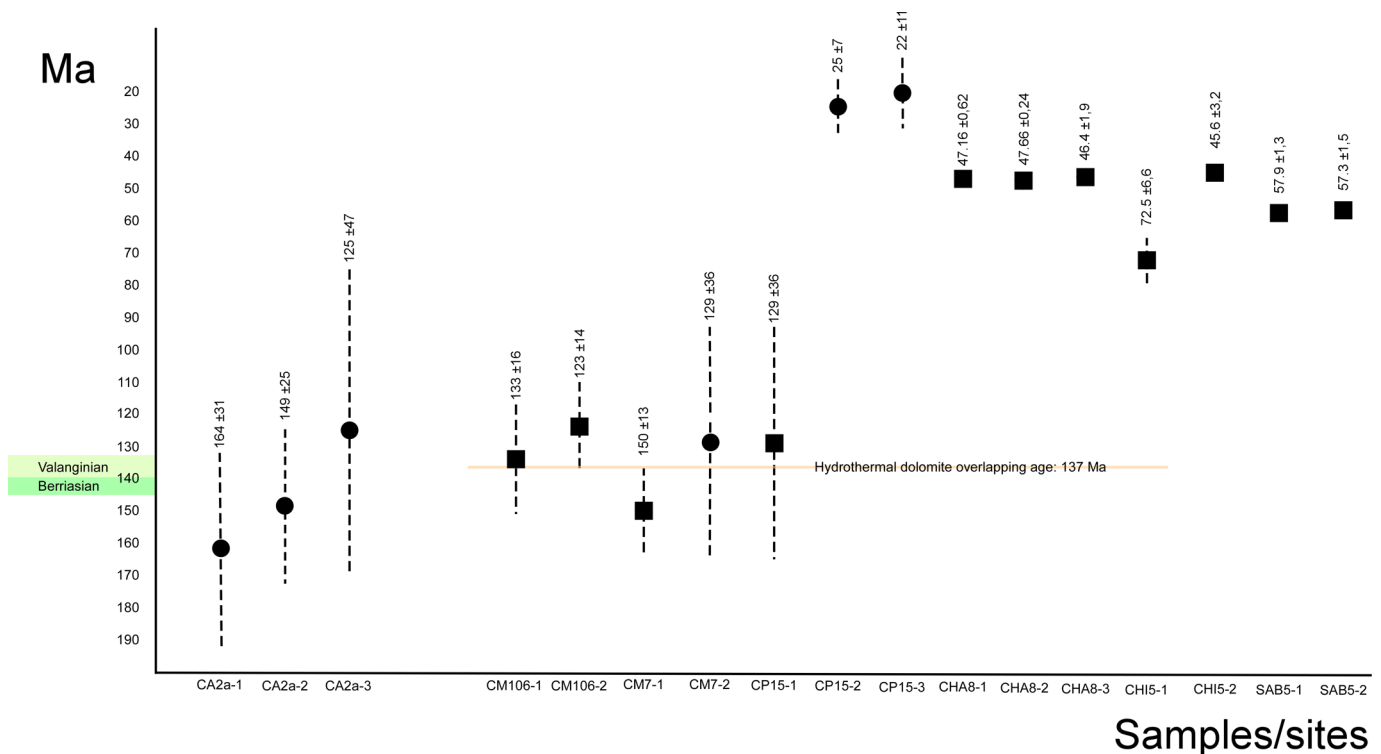


Fig. 7 - Diagram representing the measured radiometric U-Pb ages, with the corresponding 2σ errors. Calcite (black circles) and dolomite (black squares) spot analyses are distinguished. The common overlapping age of hydrothermal carbonates is evidenced; this is consistent with the latest Berriasian-Valanginian time interval proposed by Barale et al. (2016b).

interpreted as remnants of microbial tissues and thus regarded as evidence of microbial involvement in carbonate precipitation (e.g., Beauchamp and Savard, 1992; Campbell et al., 2002; Agirrezabala, 2009; Guo X. and Chafetz, 2012). Pyrite, locally associated with type-5 dolomite, is commonly considered as a byproduct of microbial-related carbonate precipitation, deriving from coupled sulphate reduction and organic compounds oxidation (e.g., Berner, 1985). Finely-crystalline, granular, carbonate cements are commonly interpreted as linked with microbial activity (e.g., Guo L. and Riding, 1994; Cavagna et al., 1999; Riding, 2000; Anadón et al., 2013).

Generally, carbonates including dolomites are excellent archives for lipid biomarkers, since lipid biomarkers, especially in authigenic carbonates, are protected from degradation during diagenesis. High thermal maturity, however, can easily modify, and at worst, erases the lipid biomarkers. Since the temperatures were at least between 170 to 260°C during hydrothermal dolomite precipitation and even higher during Alpine orogenesis, lipids were heavily affected by temperature. The overall content of lipids were very low and contained only some minor n-alkanes, but no evidence for any microbial-derived lipid biomarkers, such as terminally-branched fatty acids or isoprenoid hydrocarbons, which are often preserved in other microbial carbonates (Birgel et al., 2008b; Heindel et al., 2018). The absence of both groups of compounds in the studied samples could indicate that bacteria or archaea were not involved in dolomite precipitation. Alternatively, the signals were lost during thermal maturity, which is most likely. At the same time, the absence of oil-bearing fluid inclusions and the low content of n-alkanes suggests that the black material is not related to secondary hydrocarbon migration together with the hydrothermal fluids.

We suggest that the intercalation of Dol5 dolomite rims within coarsely-crystalline, high-temperature dolomite cements reflects changes in the functioning of the hydrothermal system. The following model is proposed (Fig. 8): during periods of hydrothermal activity, high-temperature fluids were expelled, and inorganic precipitation of Dol4 dolomite took place. These were followed by short periods of hydrothermal quiescence when upflow of high-temperature fluids was considerably reduced, allowing downward infiltration of seawater within the upper part of the hydrothermal system. The mixing with seawater sensibly lowered the fluid temperature, allowing thermophilic microbial communities to colonize the free surfaces of earlier hydrothermal cements (hyperthermophilic microbial life is reported with temperature up to 120 °C, though it could survive for short periods at even higher temperatures; Blöchl et al., 1997; Kashefi and Lovley, 2003). At the time of the dolomitization event, the burial depth of this part of the succession should not exceed 200-300 meters, corresponding to the thickness of the Jurassic carbonates. Nevertheless, microbial organisms are known to live in sub-seafloor environments at depth of more than 120 meters in hydrothermal vent systems (Kimura et al., 2003) and of several hundred meters in sediments (e.g., Parkes et al., 2000; d'Hondt et al., 2002). A similar model has been proposed by Agirrezabala (2009) in Middle Cretaceous hydrothermal vents from the Basque-Cantabrian Basin, and by Anadón et al. (2013) in Holocene hydrothermal-vent carbonates from Santorini, in which periods of hydrothermal activity and inorganic precipitation of fibrous aragonite alternated with periods of reduced hydrothermal flow allowing the growth of microbial mats.

Blackened host rock portions and the thin, carbonaceous-matter-filled veinlets, document upward migration of limited amounts of hydrocarbons, generated by forced maturation of

the organic-rich beds at the top of the Triassic succession. Hydrocarbon formation at shallow burial depth, due to forced maturation driven by hot fluids, has been documented in modern hydrothermal vents (Einsele et al., 1980; Simoneit and Lonsdale, 1982; Rushdi and Simoneit, 2002a; 2002b). Such hydrocarbons could have sustained for brief periods and in a restricted, favourable area, the metabolic activity of microbial consortia, leading to the colonization of the free surfaces of earlier cement rims within open fractures and cavities.

Sr isotopes

$^{87}\text{Sr}/^{86}\text{Sr}$ values of dolomitized rocks and dolomite cements range between 0.7077 and 0.7102, with most of the values above 0.7080 (Fig. 5). These values are systematically higher than those of seawater coeval with the dolomitization event: $^{87}\text{Sr}/^{86}\text{Sr}$ seawater compositions for the late Berriasian-Valanginian interval range between 0.70724 and 0.70739 (McArthur et al., 2007). High $^{87}\text{Sr}/^{86}\text{Sr}$ values in hydrothermal dolomites are generally interpreted as evidence of fluid interactions with crystalline or siliciclastic rocks (e.g., Duggan et al., 2001; Vandeginste et al., 2005; Shah et al., 2012) and consequent fluid enrichment in radiogenic ^{87}Sr derived from ^{87}Rb largely contained in feldspars, micas and clay minerals (Banner, 1995).

δD , $\delta^{18}\text{O}$ and noble gas isotopes of fluid inclusions-hosted water

The hydrogen isotope composition of inclusion-hosted water measured in both replacement dolomite and dolomite cement, are characterized by remarkably negative values (about -70‰ to -50‰). These values are much lower than expected for fluids that ultimately originated from sea water (Barale et al., 2016b). Similar values for δD of hydrothermal dolomites are reported in the literature and explained by several processes including 1) contribution of metamorphic/magmatic fluid (e.g., Garaguly et al., 2018); 2) high degree of evaporation of seawater (e.g., Holser, 1979; Nesbitt and Prochaska, 1997); 3) mixing with meteoric water (e.g., Yang et al., 1995). Modification of the original fluid as a result of contribution of magmatic water (δD range from -85‰ to -55‰, Taylor, 1974) is unlikely because there is no evidence for magmatic activity. In addition, the noble gas isotope composition points to crustal fluids with no significant magmatic/mantle-like component as the helium isotope ratios range from 0.02 to 0.07 Ra (average crustal values are about 0.08Ra, and $^3\text{He}/^4\text{He}$ ratios in granite range from 0.001 to 0.086Ra; Ballentine and Burnard, 2002). Some studies invoked high degrees of evaporation of sea water to explain the relatively low δD values found in dolomite (e.g., -98‰ to -50‰, Nesbitt and Prochaska, 1998). However, in this region there is no evidence of the development of a hypersaline environment in the Early Cretaceous to support this scenario. Similarly, no stratigraphic or petrographic evidence exists which could indicate subaerial conditions and involvement of meteoric waters which also could explain the low δD values.

The interaction with silicate minerals containing hydrogen (e.g., micas, clay minerals) would shift the hydrogen isotope composition of a primary seawater toward more negative values. The hydrogen isotope composition of crystalline rocks (containing biotite, amphiboles) varies generally between -80‰ and -50‰ (Clark and Fritz, 1997), while clay minerals (e.g., smectite, illite) have δD values between -65 and -50‰ (e.g., Primmer and Shaw, 1991). Extensive fluid-rock interac-

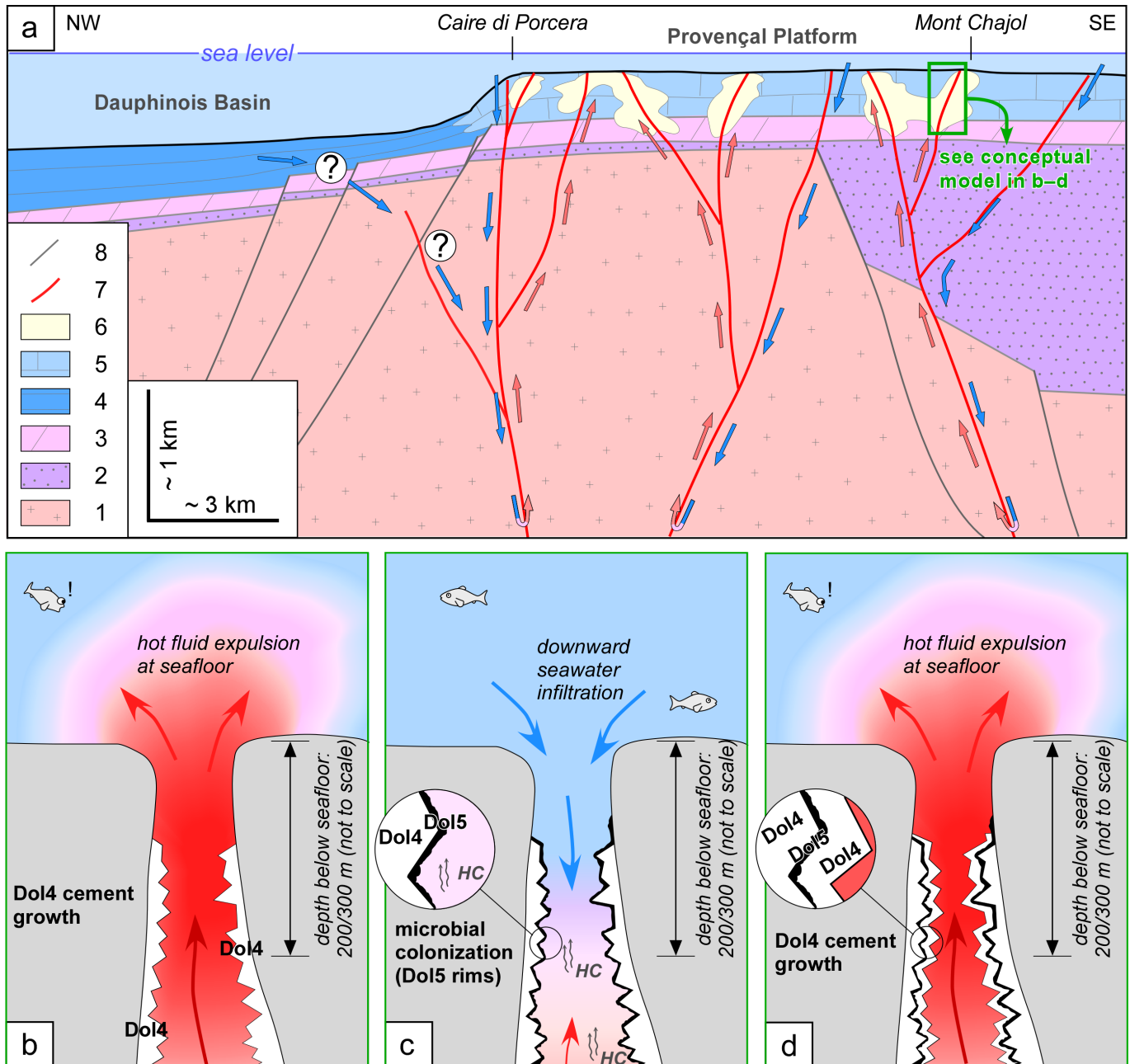


Fig. 8-. a) Conceptual model of hydrothermal system functioning, modified from Barale et al. (2016). Blue arrows represent cold descending fluids, whereas red arrows represent hot ascending fluids. 1- Argentera Massif crystalline basement. 2- Permian-Early Triassic siliciclastic deposits. 3- Middle-Late Triassic succession. 4- Jurassic Dauphinois hemipelagic succession. 5- Middle Jurassic–Berriasian Provençal carbonates (Garbella Limestone). 6- Dolomitized bodies. 7- Active faults. 8- Inactive faults. b-d) Proposed conceptual model (not to scale) of Dol5 precipitation in the Monte Chajol area (see position in a). b) Intense hydrothermal activity: high-temperature fluids are expelled through open fractures and inorganic precipitation of Dol4 dolomite takes place. c) Short period of quiescence of the hydrothermal system: the upflow of high-temperature fluids is considerably reduced allowing downward infiltration of seawater, which sensibly lowers the temperature of fluids within the upper part of the hydrothermal system. Thermophilic microbial communities, feeding on small quantities of hydrocarbons (HC) accompanying the ascending hydrothermal fluids, colonize the free surfaces of earlier hydrothermal cements, forming the thin, organic-rich Dol5 rim. d) Resumption of intense hydrothermal activity: high-temperature fluids are again expelled and growth of Dol4 dolomite resumes on previously formed Dol5 rims.

tion has indeed been already considered as a key process that modified the oxygen isotope composition of dolimitizing fluids (Barale et al., 2016b), shifting their $\delta^{18}\text{O}$ toward more positive values. Assuming interaction of the fluids with clay minerals at around 200°C , and considering the isotope fractionation of the illite/smectite-water system (Capuano, 1992), the fluid composition would show a hydrogen isotope composition comparable to the measured δD values. Although clay-

rich units are found in the stratigraphic sequence (e.g., the Permian succession), it is unknown if they could contain an amount of clay minerals sufficient to produce such a degree of isotope exchange.

The measured $\delta^{18}\text{O}$ values in the fluid inclusions-hosted water show less positive values with respect to the oxygen isotope composition calculated for parent fluid by combining carbonate oxygen isotope composition and precipitation tem-

peratures obtained by fluid inclusion microthermometry (calculated parent fluid composition: +11.2 to +14.9‰ SMOW, see above). Since the microthermometry data of Barale et al. (2016b) are reliable, lacking any evidence of post-entrapment necking or stretching of the fluid inclusions, the only possible explanation for such difference is that the oxygen isotopes of the fluid inclusions were re-equilibrated with the host dolomite at some time after its precipitation.

The hydrogen isotope compositions of fluid inclusions-hosted water in sparry calcite are more negative than those in dolomite, suggesting that calcite might have had a different origin. Moreover, by plotting them together with oxygen isotope compositions (Fig. 6), it becomes apparent that the calcite samples fall very close to the global meteoric water line (GMWL; Dansgaard, 1964), suggesting a meteoric origin of the parent fluids. Differently from the hydrothermal dolomite cements, in the meteoric calcite cements re-equilibration could not have occurred due to the lower formation temperature and possibly to its much younger age (see below, in the Discussion section).

Clumped C-O Isotopes

The temperatures calculated based on $\Delta 47$ on 4 samples of Dol3 and Dol 4 cements (Dol 3, Refrey Zone: 309°C; Dol3, Entracque Unit: 258°C, 351°C; Dol4, Upper Roya Unit: 325°C) are significantly higher than temperatures obtained from fluid inclusion microthermometry on the same phases (Dol3: 170-240°C; Dol4: 190-260°C; Barale et al., 2016b). For this reason, we conclude that the original $\Delta 47$ signal of hydrothermal dolomites was reset during subsequent Alpine heating. The same is assumed for Cc1 calcite, which shows analogous $\Delta 47$ temperatures on two samples from the Entracque Unit (270°C, 292°C).

The calculated $\Delta 47$ temperatures are consistent with the middle anchizonal Alpine heating inferred, based on illite and chlorite ‘crystallinity’ indices, for the Refrey Zone and the Upper Roya Unit (Piana et al., 2014), which can be reasonably extended also to the adjoining Entracque Unit.

U-Pb datings

The non-dolomitized portions of the sample Ca2a were analyzed to test the reliability of the U-Pb method in our study area. The uncertainty of these datings is unfortunately considerable; however, they are not in contrast with the Late Jurassic age of the corresponding stratigraphic interval. Among the dolomitized samples, two different clusters of ages are distinguishable in Fig. 7. The ages of the first cluster are between 148 and 124 Ma. Taking in account the error bars, a common overlapping age around 137 Ma is present. This fits with the timing proposed by Barale et al. (2016b), who, based on stratigraphic evidence, constrained the dolomitization event to the latest Berriasian-Valanginian.

The ages of the second cluster are much younger, between 72 and 24 Ma, and document that reopening events must have occurred following the dolomitization event. In some cases they occurred through a recrystallization process, and the sample CP15 is quite illustrative of such process. It is a lithoclastic floatstone with dolomitized clasts of reworked dolomitized Garbella limestones in a microsparitic matrix: the dolomite of the clasts (CP15-1) was not recrystallized and retained the Cretaceous primary ages of the dolomitization, whereas the primary calcite micrite matrix was recrystallized to microsparite and the U-Pb system was reset. In other cases,

a reopening occurred without any observable recrystallization or dissolution. CHA8-1 and CHA8-3 are Dol4 cements, without any evidence for recrystallization or dissolution, and the same is true for the CHA8-2 dark, organic-rich Dol5 dolomite rim. Despite being referable to the Early Cretaceous dolomitization, they gave very precise ages around 47-46 Ma. In our interpretation, these ages, and the ages of the second cluster, do not represent the primary ages of formation, but could have a geological meaning, being in some ways possibly related to younger events that re-opened the U-Pb system. A regional unconformity at the base of the Alpine Foreland Basin succession cuts the Mesozoic European palaeomargin succession and corresponds to a hiatus spanning the latest Cretaceous-Middle Eocene. It is associated with evidence for a subaerial emersion related to the forebulge uplift (e.g., Ford et al., 1999; Varrone and Clari, 2003): the related influx of meteoric fluids could have locally reset or partially reopened the U-Pb system of some dolomite cements, resulting in the ages between 72.4 and 45.6 Ma. The two ages of 24.7 ± 6.9 and 26 ± 11 Ma of the sample CP15 could be related to the hydrothermal circulation in a transcurrent tectonic setting that, a few kilometers to the west of the study area, led to the formation of the Valdieri Marble, which has been recently dated by Bertok et al. (2019) to the Early Oligocene (31.6 - 30 Ma). Alternatively, these two relatively younger ages could be related to recrystallization during a subsequent transtensional tectonic regime developed along the Western Ligurian Alps border and adjacent syn-orogenic basins. This regime, which persisted through the Rupelian and early Chattian, induced the uplifting and cooling of the Ligurian Alps tectonic stack (Bertotti et al., 2006; Maino et al., 2013), with the coeval formation of localized fault-bounded basins characterized by strong subsidence rates (Mutti et al., 1995; Ghibaudo et al., 2019).

DISCUSSION

The new results discussed in the above chapters confirm the overall picture of the hydrothermal system functioning described in Barale et al. (2016b), in particular:

- The inferred age of the hydrothermal event, constrained to the latest Berriasian-Valanginian based on stratigraphic evidence, has been confirmed by U-Pb datings on hydrothermal dolomite. A cluster of U-Pb ages between 148 and 124 Ma is present, with an overlapping age around 137 Ma (taking into account the relevant errors), which corresponds to the Valanginian.
- The hypothesis of a deep circulation of the hydrothermal fluids within the crystalline basement of the Argentera Massif and the overlying Permian-Early Triassic siliciclastic succession is supported by the $^{87}\text{Sr}/^{86}\text{Sr}$ values of hydrothermal dolomites. These are systematically higher than $^{87}\text{Sr}/^{86}\text{Sr}$ values of Mesozoic seawaters, and can be explained with prolonged interaction of fluids with feldspar and/or mica-bearing rocks. This hypothesis of prolonged interaction with crystalline and terrigenous rocks seems to be also supported by the strongly negative hydrogen isotope composition (δD) of inclusion-hosted water in hydrothermal dolomites.
- The hydrothermal system pulsing character was already highlighted by several lines of evidence, including polyphase cavity opening, polyphase breccias, and presence of laminated internal sediments within cavities (Barale et al., 2016b). A new evidence is provided by the newly described, organic matter-rich dolomite rims locally in-

terposed within coarse crystalline hydrothermal dolomite cements. These are here interpreted as remnants of ephemeral microbial communities which could colonize open fractures within the upper part of the hydrothermal conduits, during periods of reduced upflow of hot fluids and contextual downward seawater infiltration (Fig. 8). Sparry calcite is the last phase of void filling, and was considered by Barale et al. (2016b) as a product of the last stages of hydrothermal circulation, even though no data about precipitation temperature were available. One U-Pb radiometric age obtained on a void-filling sparry calcite (CM7-2; 129 ± 36 Ma) is consistent with the age of the hydrothermal dolomitization and thus supports this interpretation. On the other hand, the new δD and $\delta^{18}O$ fluid inclusion data in other sparry calcite cements (samples CM16, KIAM1, SAB14) point to a meteoric origin. As discussed above, the dolomitized Provençal succession underwent a generalized uplift and subaerial exposure in the latest Cretaceous-Middle Eocene; the related influx of meteoric water probably caused the reopening of the U-Pb system of some Early Cretaceous hydrothermal dolomites. Based on these considerations, it is here proposed that in the study area at least two generations of void filling sparry calcite occur (though not distinguishable from a petrographic point of view; Barale et al., 2016b). The first sparry calcite phase is probably a high temperature product and related to the Early Cretaceous hydrothermal circulation. This is also supported by the presence of calcite cements predating the deposition of internal sediments in cavities (see Fig. 13d in Barale et al., 2016b). A later sparry calcite phase precipitated from meteoric waters circulating in the dolomitized Provençal succession during subaerial exposure related to the latest Cretaceous-Middle Eocene regional uplift.

The results presented in this paper allow a few considerations on the preservation potential, during orogenic processes, of some geochemical signals that are increasingly utilized in the study of diagenetic carbonates. The dolomitized Provençal succession was affected during Alpine orogeny by a middle anchizonal heating (Piana et al., 2014; data from the Refrey Zone and Upper Roya Unit, here assumed to be valid also for the adjoining Entracque Unit). This heating seems to have invariably reset the primary clumped isotope signal of both dolomites and calcites, whose $\Delta 47$ signatures were probably altered through recrystallization and/or reordering processes (Stolper and Eiler, 2015). On the other hand, the original U-Pb signal has been preserved on a part of the analyzed dolomites and calcites, notwithstanding later Alpine heating. The reopening of the U-Pb system recorded by other samples can be put in relation with both low temperature regional events (meteoric influx during latest Cretaceous-Middle Eocene uplift) and higher temperature Alpine events.

CONCLUSIONS

The reported case study shows that in complex settings, where subsequent deformation events hinder the direct observation of all the elements of a fossil hydrothermal system, its general functioning can be unraveled by adopting a multidisciplinary approach integrating several analytical techniques. This provides information on the age of hydrothermal processes and the physico-chemical and isotopic characters of hydrothermal fluids. This in turn allows the reconstruction of the origin and interaction of the fluids with the host rocks,

their circulation pathways, and the burial depth at which the hydrothermal processes took place.

This multi-analytical approach allowed us to document a large-scale hydrothermal circulation that affected the Mesozoic Provençal succession during the Valanginian, related to seawater strongly heated and compositionally modified by deep circulation within crystalline rocks. The hydrothermal circulation was hosted by deep-rooted faults and related fracture systems, and is indirect evidence of a significant earliest Cretaceous fault activity in the southern part of the Alpine Tethys European continental margin.

The Valanginian age proposed for the studied hydrothermal dolomitization is at least 15 Myr older than the Aptian to Late Cretaceous Marguareis faulting activity reported by Bertok et al. (2012) in the nearby Ligurian Briançonnais Domain. However, the faults and fracture systems that conveyed the studied hydrothermal fluids could be tentatively related to the same tensional or transtensional stress field that affected the easternmost portion of the Iberia crustal block in the late Early Cretaceous (Ford and Vergés, 2020) and possibly also the adjoining SW part of the Briançonnais domain along the Paleo-European margin. In the nearby eastern part of the Iberia block, the Early Cretaceous continental margin was going to experience indeed a significant crustal thinning with related HT metamorphism, which occurred between 110 and 90 Ma (Clerc and Lagabrielle 2014; Clerc et al., 2015). In the same period, the overlying Mesozoic carbonate successions were affected by hydrothermal activity at relatively shallow burial depth (e.g., Basque-Cantabrian Basin: López-Horgue et al., 2010. Chañons Béarnais: Incerpi et al., 2020a; Motte et al., 2021).

The studied hydrothermal fluid circulation - and related fracturing - could be considered as a precursor of the tectonic processes that led to the development of the above-described deep-rooted faults on the European margin side. These processes anticipated the main late Early Cretaceous faulting events, which are also recorded in other parts of the Provençal Domain (e.g., Dardeau and de Graciansky, 1987; de Graciansky and Lemoine, 1988; Hibsich et al., 1992; Montenat et al., 1997; 2004; Friès and Parize, 2003; Masse et al., 2009). In this sense, they could be considered as a shallow crustal evidence of the Valanginian to Aptian extensional and transtensional tectonic structures (e.g., Angrand et al., 2020; Ford and Vergés, 2020) that led to the individuation of a major transform zone placed between the Iberia and Europe continental margins (see paleogeographic maps in Stampfli et al., 2002; Handy et al., 2010; Tavani et al., 2018), likely characterized by interconnected extensional and strike slip basins developed in the easternmost segment of the Iberia-Europe transition zone.

ACKNOWLEDGEMENTS

First of all, we want to remember our friend and colleague Marco Beltrando. We shared with him the early stages of the researches presented in this paper, and his enthusiasm and passion have been and continue to be an inspiration to us.

We thank the reviewers Alessandro Decarlis and Mikel A. López-Horgue for their useful comments. This research was supported by the University of Torino (ex 60% funds to C. Bertok and A. d'Atri) and by the CNR-IGG (National Research Council of Italy, Institute of Geosciences and Earth Resources, Torino unit). A financial contribution by the International Association of Sedimentologists to L. Barale (IAS Grant Scheme Award, 2nd session 2012) is gratefully acknowledged.

REFERENCES

- Agirrezabala L.M., 2009. Mid-Cretaceous hydrothermal vents and authigenic carbonates in a transform margin, Basque-Cantabrian Basin (western Pyrenees): a multidisciplinary study. *Sedimentology*, 56 (4): 969-996.
- Anadón P., Canet C. and Friedrich W.L., 2013. Aragonite stromatolitic buildups from Santorini (Aegean Sea, Greece): Geochemical and palaeontological constraints of the caldera palaeoenvironment prior to the Minoan eruption (ca 3600 yr bp). *Sedimentology*, 60 (5): 1128-1155.
- Angrand P., Mouthereau F., Masini E. and Asti R., 2020. A reconstruction of Iberia accounting for Western Tethys-North Atlantic kinematics since the late-Permian-Triassic. *Solid Earth*, 11: 1313-1332.
- Ballentine C.J. and Burnard P.G., 2002. Production, release and transport of noble gases in the continental crust. *Rev. Miner. Geochem.*, 47 (1): 481-538.
- Banner J.L., 1995. Application of the trace element and isotope geochemistry of strontium to studies of carbonate diagenesis. *Sedimentology*, 42: 805-824.
- Barale L., 2014. The Meso-Cenozoic stratigraphic successions adjoining the Argentera Massif: stratigraphic, sedimentologic and diagenetic evidence of syndepositional tectonics. Unpubl. PhD Thesis, Univ. Torino, 240 pp.
- Barale L., Bertok C., d'Atri A., Domini G., Martire L. and Piana F., 2013. Hydrothermal dolomitization of the carbonate Jurassic succession in the Provençal and Subbriançonnais Domains (Maritime Alps, North-Western Italy). *C.R. Geosci.*, 345: 47-53.
- Barale L., Bertok C., d'Atri A., Martire L. and Piana F., 2017. Stratigraphy, sedimentology and syndepositional tectonics of the Jurassic-Cretaceous succession at the transition between Provençal and Dauphinois domains (Maritime Alps, NW Italy). *Riv. It. Paleont. Strat.*, 123 (3): 355-378.
- Barale L., Bertok C., d'Atri A., Martire L., Piana F. and Domini G., 2016a. Geology of the Entracque-Colle di Tenda area (Maritime Alps, NW Italy). *J. Maps*, 12: 359-370.
- Barale L., Bertok C., Salih Talabani N., d'Atri A., Martire L., Piana F. and Préat A., 2016b. Very hot, very shallow hydrothermal dolomitization: an example from the Maritime Alps (NW Italy-SE France). *Sedimentology*, 63: 2037-2065.
- Beauchamp B. and Savard M., 1992. Cretaceous chemosynthetic carbonate mounds in the Canadian Arctic. *Palaios*, 7: 434-450.
- Benjakul R., Hollis C., Robertson H.A., Sonnenthal E.L. and Whitaker F.F., 2020. Understanding controls on hydrothermal dolomitization: insights from 3D reactive transport modelling of geothermal convection. *Solid Earth*, 11: 2439-2461.
- Bernasconi S.M., Müller I.A., Bergmann K.D., Breitenbach S.F., Fernandez A., Hodell D.A., Jaggi M., Meckler A.N., Millan I. and Ziegler M., 2018. Reducing uncertainties in carbonate clumped isotope analysis through consistent carbonate-based standardization. *Geochem. Geophys. Geosyst.*, 19 (9): 2895-2914.
- Berner R.A., 1985. Sulphate reduction, organic matter decomposition and pyrite formation. *Phil. Trans. R. Soc. London*, 315: 25-38.
- Bersezio R. and d'Atri A., 1986. Nota preliminare sulla stratigrafia del Trias medio della copertura sedimentaria del massiccio dell'Argentera nell'alta Valle Roja. *Atti Acc. Naz. Lincei*, 80: 135-144.
- Bertok C., Barale L., d'Atri A., Martire L., Piana F., Rossetti P. and Gerdes A., 2019. Unusual marbles in a non-metamorphic succession of the SW Alps (Valdieri, Italy) due to early Oligocene hydrothermal flow. *Int. J. Earth Sci.*, 108: 693-712.
- Bertok C., Martire L., Perotti E., d'Atri A. and Piana F., 2012. Kilometre-scale palaeoscarpments as evidence for Cretaceous syndimentary tectonics in the External Briançonnais domain (Ligurian Alps, Italy). *Sedim. Geol.*, 251: 58-75.
- Bertotti G., Mosca P., Juez J., Polino R. and Dunai T., 2006. Oligocene to Present kilometres scale subsidence and exhumation of the Ligurian Alps and the Tertiary Piedmont Basin (NW Italy) revealed by apatite (U-Th)/He thermochronology correlation with regional tectonics. *Terra Nova*, 18 (1): 18-25.
- Birgel D., Elvert M., Han X. and Peckmann J., 2008a. ¹³C-depleted biphytanic diacids as tracers of past anaerobic oxidation of methane. *Org. Geochem.*, 39: 152-156.
- Birgel D., Himmler T., Freiwald A. and Peckmann J., 2008b. A new constraint on the antiquity of anaerobic oxidation of methane: Late Pennsylvanian seep limestones from southern Namibia. *Geology*, 36: 543-546.
- Birgel D., Thiel V., Hinrichs K.-U., Elvert M., Campbell K.A., Reintner J., Farmer J.D. and Peckmann J., 2006. Lipid biomarker patterns of methane-seep microbialites from the Mesozoic convergent margin of California. *Org. Geochem.*, 37: 1289-1302.
- Blöchl E., Rachel R., Burggraf S., Hafenbradl D., Jannasch H.W. and Stetter K.O., 1997. *Pyrolobus fumarii*, gen. and sp. nov., represents a novel group of archaea, extending the upper temperature limit for life to 113°C. *Extremophiles*, 1: 14-21.
- Boni M., Parente G., Bechstädt T., De Vivo B. and Iannace A., 2000. Hydrothermal dolomites in SW Sardinia (Italy): evidence for a widespread late-Variscan fluid flow event. *Sedim. Geol.*, 131: 181-200.
- Campbell K.A., Farmer J.D. and Des Marais D., 2002. Ancient hydrocarbon seeps from the Mesozoic convergent margin of California: carbonate geochemistry, fluids and palaeoenvironments. *Geofluids*, 2: 63-94.
- Capuano R.M., 1992. The temperature dependence of hydrogen isotope fractionation between clay minerals and water: Evidence from a geopressured system. *Geochim. Cosmochim. Acta*, 56 (6): 2547-2554.
- Carraro F., Dal Piaz G.V., Franceschetti B., Malaroda R., Sturani C. and Zanella E., 1970. Note Illustrative della Carta Geologica del Massiccio dell'Argentera alla scala 1: 50.000. *Mem. Soc. Geol. It.*, 9: 557-663.
- Cavagna S., Clari P. and Martire L., 1999. The role of bacteria in the formation of cold seep carbonates: geological evidence from Monferrato (Tertiary, NW Italy). *Sedim. Geol.*, 126: 253-270.
- Clark I. and Fritz P., 1997. *Environmental isotopes in hydrogeology*. Lewis, New York, 352 pp.
- Clerc C. and Lagabrielle Y., 2014. Thermal control on the modes of crustal thinning leading to mantle exhumation: Insights from the Cretaceous Pyrenean hot paleomargins. *Tectonics*, 33: TC003471.
- Clerc C., Lahfid A., Monié P., Lagabrielle Y., Chopin C., Poujol M., Boulvais P., Ringenbach J.-C., Masini E. and de St Blanquat M., 2015. High-temperature metamorphism during extreme thinning of the continental crust: a reappraisal of the north Pyrenean paleo-passive margin. *Solid Earth Discuss.*, 6: 1-61.
- Coplen T.B., de Bièvre P., Krouse H.R., Vocke R.D., Gröning M. and Rozanski K., 1996. Ratios for light-element isotopes standardized for better interlaboratory comparison, *Eos Trans. AGU*, 77 (27): 255-255.
- Czuppon G., Ramsay R.R., Özgenc I., Demény A., Gwalani L.G., Rogers K., Eves A., Papp L., Palcsu L., Berkesi M. and Downes P.J., 2014. Stable (H, O, C) and noble-gas (He and Ar) isotopic compositions from calcite and fluorite in the Speewah dome, Kimberley region, western Australia: implications for the conditions of crystallization and evidence for the influence of crustal-fluid mixing. *Miner. Petrol.*, 108: 759-775.
- Dansgaard W., 1964. Stable isotopes in precipitation. *Tellus*, 16: 436-468.
- Dardeau G. and de Graciansky P.C., 1987. Indices d'une tectonique synsédimentaire d'âge crétacé inférieur dans la basse vallée de l'Estéron (Alpes-Maritimes) et conséquences géodynamiques. *Bull. Soc. Géol. Fr.*, 3: 1207-1210.
- d'Atri A., Piana F., Barale L., Bertok C. and Martire L., 2016. Geological setting of the southern termination of Western Alps. *Int. J. Earth Sci.*, 105 (6): 1831-1858.
- Davies, G.R. and Smith, L.B.Jr., 2006. Structurally controlled hydrothermal dolomite reservoir facies: An overview. *AAPG Bull.*, 90: 1641-1690.
- Debelmas J. and Kerckhove C., 1980. Les Alpes franco-italiennes. *Géol. Alp.*, 56: 21-58.
- Debelmas J. and Lemoine M., 1970. The Western Alps: paleogeography and structure. *Earth-Sci. Rev.*, 6: 221-256.

- de Graciansky P.C. and Lemoine M., 1988. Early Cretaceous extensional tectonics in the southwestern French Alps: a consequence of North-atlantic rifting during Tethyan spreading. *Bull. Soc. Géol. Fr.*, 4: 733-737.
- Demény A., Czuppon G., Kern Z., Leél-Óssy S., Németh A., Szabó M., Tóth M., Wu C.-C., Shen C.-C., Molnár M., Németh T., Németh P. and Óvári M., 2016. Recrystallization-induced oxygen isotope changes in inclusion-hosted water of speleothems - Palaeoclimatological implications, *Quatern. Int.*, 415: 25-32.
- Denniston R.F., Asmerom Y., Polyak V.Y., McNeill D.F., Klaus J.S., Cole P. and Budd A.F., 2008. Caribbean chronostratigraphy refined with U-Pb dating of a Miocene coral. *Geology*, 36 (2): 151-154.
- D'Hondt S., Rutherford S. and Spivack A.J., 2002. Metabolic activity of subsurface life in deep-sea sediments. *Science*, 295: 2067-2070.
- Duggan J.P., Mountjoy E.W. and Stasiuk L.D., 2001. Fault-controlled dolomitization at Swan Hills Simonette oil field (Devonian), deep basin west-central Alberta, Canada. *Sedimentology*, 48: 301-323.
- Dumont T., Schwartz S., Guillot S., Simon-Labrie T., Tricart P. and Jourdan S., 2012. Structural and sedimentary records of the Oligocene revolution in the Western Alpine arc. *J. Geodyn.*, 56-57: 18-38.
- Einsele G., Gieskes J.M., Curray J., Moore D.M., Aguayo E., Aubry M.-P., Fornari D., Guerrero J., Kastner M., Kelts K., Lyle M., Matoba Y., Molina-Cruz A., Niemitz J., Rieda J., Saunders A., Chrader H., Simoneit B. and Vacquier V., 1980. Intrusion of basaltic sills into highly porous sediments, and resulting hydrothermal activity. *Nature*, 283: 441-445.
- Elisha B., Nuriel P., Kylander-Clark A. and Weinberger R., 2020. Towards in-situ U-Pb dating of dolomites, *Geochronol. Discuss.* [preprint], <https://doi.org/10.5194/gchron-2020-19>, in review, 2020.
- Faure-Muret A., 1955. Études géologiques sur le massif de l'Argentera-Mercantour et ses enveloppes sédimentaires. *Mém. Carte Géol. France*, Paris, 336 pp.
- Faure-Muret A., Fallot P. and Lanteaume M., 1967. Carte géologique de la France à 1:50.000, feuille St-Martin-Vésubie - Le Boréon (947). *Bureau Rech. Géol. Min., Orléans*.
- Fernandez A., Müller I.A., Rodriguez-Sanz L., van Dijk I., Looser N. and Bernasconi S.M., 2017. Reassessment of the precision of carbonate clumped isotope measurements: implications for calibrations and paleoclimate reconstructions. *Geochem. Geophys. Geosyst.*, 18: 4375-4386.
- Ferry J.M., Passey B.H., Vasconcelos C. and Eiler J.M., 2011. Formation of dolomite at 40-80°C in the Latemar carbonate buildup, Dolomites, Italy, from clumped isotope thermometry. *Geology*, 39: 571-574.
- Ford M. and Vergés J., 2020. Evolution of a salt-rich transtensional rifted margin, eastern North Pyrenees, France. *J. Geol. Soc. London*, 178: jgs2019-157.
- Ford M., Lickorish W.H. and Kusznir N.J., 1999. Tertiary foreland sedimentation in the Southern Subalpine Chains, SE France: a geodynamic appraisal. *Basin Res.*, 11: 315-336.
- Friès G. and Parize O., 2003. Anatomy of ancient passive margin slope systems: Aptian gravity-driven deposition on the Voconian palaeomargin, Western Alps, south-east France. *Sedimentology*, 50: 1231-1270.
- Garaguly I., Varga A., Raucsik B., Schubert F., Czuppon G. and Frei R., 2018. Pervasive early diagenetic dolomitization, subsequent hydrothermal alteration, and late stage hydrocarbon accumulation in a Middle Triassic carbonate sequence (Szeged Basin, SE Hungary). *Mar. Petrol. Geol.*, 98: 270-290.
- Gerdes A. and Zeh A., 2006. Combined U-Pb and Hf isotope LA-(MC-) ICP-MS analyses of detrital zircons: comparison with SHRIMP and new constraints for the provenance and age of an Armorican metasediment in Central Germany. *Earth Planet. Sci. Lett.*, 249: 47-62.
- Gerdes A. and Zeh A., 2009. Zircon formation versus zircon alteration - New insights from combined U-Pb and Lu-Hf in-situ LA-ICP-MS analyses of Archean zircons from the Limpopo Belt. *Chem. Geol.*, 261 (3-4): 230-243.
- Ghibaud G., Massari F., Chiambretti I., d'Atri A. and Fornaciari E., 2019. Birth and tectono-sedimentary evolution of the Tertiary Piedmont Basin (NW Italy). *J. Medit. Earth Sci.*, 11: 5-112.
- Gidon M., 1972. Les chaînons briannonnais et subbriannonnais de la rive gauche de la Stura entre le Val de l'Arma (province de Cuneo Italie). *Géol Alpine*, 48: 87-120.
- Godeau N., Deschamps P., Guihou A., Léonide P., Tendil A., Gerdes A., Hamelin B. and Girard J.P., 2018. U-Pb dating of calcite cement and diagenetic history in microporous carbonate reservoirs: Case of the Urgonian Limestone, France. *Geology*, 46: 247-250.
- Guo L. and Riding R., 1994. Origin and diagenesis of Quaternary travertine shrub fabrics, Rapolano Terme, central Italy. *Sedimentology*, 41: 499-520.
- Guo X. and Chafetz H.S., 2012. Large tufa mounds, Searles Lake, California. *Sedimentology*, 59 (5): 1509-1535.
- Haeri-Ardakani O., Al-Aasm I. and Coniglio M., 2013. Fracture mineralization and fluid flow evolution: an example from Ordovician-Devonian carbonates, southwestern Ontario, Canada. *Geofluids*, 13: 1-20.
- Handy M.R., Schmid S.M., Bousquet R., Kissling E. and Bernoulli D., 2010. Reconciling plate-tectonic reconstructions of Alpine Tethys with the geological-geophysical record of spreading and subduction in the Alps. *Earth Sci. Rev.*, 102 (3-4): 121-158.
- Hansman R.J., Albert R., Gerdes A. and Ring U., 2018. Absolute ages of multiple generations of brittle structures by U-Pb dating of calcite. *Geology*, 46 (3): 207-210.
- Heindel K., Foster W.J., Richoz S., Birgel D., Roden V.J., Baud A., Brandner R., Krystyn L., Mohtat T., Koşun E., Twitchett R.J., Reiter J. and Peckmann J., 2018. The formation of microbial-metazoan bioherms and biostromes following the late Permian mass extinction. *Gondw. Res.*, 61: 187-202.
- Hendry J.P., Gregg J.M., Shelton K.L., Somerville I.D. and Crowley S.F., 2015. Origin, characteristics and distribution of fault-related and fracture-related dolomitization: Insights from Mississippian carbonates, Isle of Man. *Sedimentology*, 62: 717-752.
- Hibsch C., Jandel D., Montenat C. and Ott d'Estevou P., 1992. Événements tectoniques crétaqués dans la partie méridionale du bassin subalpin (massif Ventoux-Lure et partie orientale de l'arc de Castellane, SE France). Implications géodynamiques. *Bull. Soc. Géol. France*, 163: 147-158.
- Hollis C., Bastesen E., Boyce A., Corlett H., Gawthorpe R., Hirani J., Rotevatn A. and Whitaker F., 2017. Fault-controlled dolomitization in a rift basin. *Geology*, 45: 219-222.
- Holser W.T., 1979. Trace elements and isotopes in evaporites. In: R.G. Burns (Ed.), *Marine minerals*. *Min. Soc. Am., Short Course Notes*, 6: 295-346.
- Honlet R., Gasparrini M., Mucchez P., Swennen R. and John C.M., 2018. A new approach to geobarometry by combining fluid inclusion and clumped isotope thermometry in hydrothermal carbonates. *Terra Nova*, 30: 199-206.
- Incerpi N., Manatschal G., Martire L., Bernasconi S.M., Gerdes A. and Bertok C., 2020a. Characteristics and timing of hydrothermal fluid circulation in the fossil Pyrenean hyperextended rift system: new constraints from the Chaînons Béarnais (W Pyrenees). *Int. J. Earth Sci.*, 109: 1071-1093.
- Incerpi N., Martire L., Manatschal G. and Bernasconi S.M., 2017. Evidence of hydrothermal fluid flow in a hyperextended rifted margin: the case study of the Err nappe (SE Switzerland). *Swiss J. Geosci.*, 110 (2): 439-456.
- Incerpi N., Martire L., Manatschal G., Bernasconi S.M., Gerdes A., Czuppon G., Palcsu L., Karner G.D., Johnson C.A. and Figueredo P.H., 2020b. Hydrothermal fluid flow associated to the extensional evolution of the Adriatic rifted margin: Insights from the pre- to post-rift sedimentary sequence (SE Switzerland, N Italy). *Basin Res.*, 32: 91-115.
- John C.M. and Bowen D., 2016. Community software for challenging isotope analysis: First applications of "Easotope" to clumped isotopes. *Rapid Comm. Mass Spectrom.*, 30: 2285-2300.

- Kashefi K. and Lovley D.R., 2003. Extending the upper temperature limit for life. *Science*, 301: 934.
- Kimura H., Asada R., Masta A. and Naganuma T., 2003. Distribution of microorganisms in the subsurface of the Manus Basin hydrothermal vent field in Papua New Guinea. *Appl. Environ. Microb.*, 69: 644-648.
- Kylander-Clark A.R.C., 2020. Expanding the limits of laser-ablation U-Pb calcite geochronology. *Geochron.*, 2: 343-354.
- Koeshidayatullah A., Corlett H., Stacey J., Swart P.K., Boyce A. and Hollis C., 2020. Origin and evolution of fault-controlled hydrothermal dolomitization fronts: A new insight. *Earth Planet. Sci. Lett.*, 541: 116291.
- Land L.S., 1985. The origin of massive dolomite. *J. Geol. Educ.*, 33: 112-125.
- Lanteaume M., 1990. Carte géologique de la France à 1:50.000, feuille Viève-Tende (948). *Bur. Rech. Géol. Min., Orléans*.
- Lavoie D. and Morin C., 2004. Hydrothermal dolomitization in the Lower Silurian Sayabec Formation in northern Gaspé - Matapédia (Québec): constraint on timing of porosity and regional significance for hydrocarbon reservoirs. *Bull. Can. Petrol. Geol.*, 52: 256-269.
- Li Q., Parrish R.R., Horstwood M.S.A. and McArthur J.M., 2014. U-Pb dating of cements in Mesozoic ammonites. *Chem. Geol.*, 376: 76-83.
- López-Horgue M.A., Iriarte E., Schröder S., Fernández-Mendiola P.A., Caline B., Corneillie H., Frémont J., Sudrie M. and Zerti S., 2010. Structurally controlled hydrothermal dolomites in Albian carbonates of the Asón valley, Basque Cantabrian Basin, Northern Spain. *Mar. Petrol. Geol.*, 27: 1069-1092.
- Luczaj J.A., 2006. Evidence against the Dorag (mixing-zone) model for dolomitization along the Wisconsin arc - A case for hydrothermal diagenesis. *AAPG Bull.*, 90 (11): 1719-1738.
- Ludwig K.R., 2009. *Isoplot/Ex Ver 3.71: a geochronological toolkit for Microsoft Excel*. Berkeley Geochron. Center Spec. Publ., Berkeley.
- Machel H.G. and Lonnee J., 2002. Hydrothermal dolomite - a product of poor definition and imagination. *Sedim. Geol.*, 152: 163-171.
- Maino M., Decarlis A., Felletti F. and Seno S., 2013. Tectono-sedimentary evolution of the Tertiary Piedmont Basin (NW Italy) within the Oligo-Miocene central Mediterranean geodynamics. *Tectonics*, 32 (3): 593-619.
- Malaroda R., 1999. L'Argentera meridionale - Memoria illustrativa della "Geological Map of Southern Argentera Massif (Maritime Alps) 1 :25 000". *Mem. Sci. Geol.*, 51-52: 241-331.
- Masse J.-P., Villeneuve M., Leonforte E. and Nizou J., 2009. Block tilting of the North Provence Early Cretaceous carbonate margin: stratigraphic, sedimentologic and tectonic data. *Bull. Soc. Géol. France*, 180: 105-115.
- McArthur J.M., Howarth R.J. and Shields G.A., 2012. Strontium isotope stratigraphy. In: F. Gredstein, J. Ogg, M. Schmitz and G. Ogg (Eds.), *The geological time scale 2012*. Elsevier, Amsterdam.
- McArthur J.M., Janssen N.M.M., Reboulet S., Leng M.J., Thirlwall M.F. and van de Schootbrugge B., 2007. Palaeotemperatures, polar ice volume, and isotope stratigraphy (Mg/Ca, $\delta^{18}\text{O}$, $\delta^{13}\text{C}$, $87\text{Sr}/86\text{Sr}$): The Early Cretaceous (Berriasian, Valanginian, Hauterivian). *Palaeogeography, Palaeoclimatology, Palaeoecology*, 248: 391-430.
- Meckler A.N., Ziegler M., Millán M.I., Breitenbach S.F.M. and Bernasconi S.M., 2014. Long-term performance of the Kiel carbonate device with a new correction scheme for clumped isotope measurements. *Rapid Comm. Mass Spectr.*, 28: 1705-1715.
- Michard A., Avigad D., Goffé B. and Chopin C., 2004. The high-pressure metamorphic front of the south Western Alps (Ubaye-Maira transect, France, Italy). *Schweiz. Miner. Petrogr. Mitt.*, 84: 215-235.
- Middleton K., Coniglio M., Sherlock R. and Frapce S.K., 1993. Dolomitization of Middle Ordovician carbonate reservoirs, Southwestern Ontario. *Bull. Can. Petrol. Geol.*, 41 (2): 150-163.
- Molli G., Crispini L., Piana F., Mosca P., Federico L. and Malusà M.G., 2010. Geology of the Western Alps-Northern Apennine junction area: a regional review. *J. Virt. Expl.*, doi: 10.3809/jvirtex.2010.00215
- Montenat C., Hibsich C., Perrier J.C., Pascaud F. and De Bretizel P., 1997. Tectonique cassante d'âge crétacé inférieur dans l'Arc de Nice (Alpes-Maritimes, France). *Géol. Alp.*, 73: 59-66.
- Montenat C., Janin M.-C. and Barrier P., 2004. L'accident du Toulourenc: une limite tectonique entre la plate-forme provençale et le Bassin vocontien à l'Aptien-Albien (SE France). *C.R. Geosci.*, 336: 1301-1310.
- Motte G., Hoareau G., Callot J.-P., Révillon S., Piccoli F., Calasou S. and Gaucher E.C., 2021. Rift and salt-related multi-phase dolomitization: example from the northwestern Pyrenees. *Mar. Petrol. Geol.*, 126: 104932.
- Mozafari M., Swennen R., Balsamo F., El Desouky H., Storti F. and Taberner C., 2019. Fault-controlled dolomitization in the Montagna dei Fiori Anticline (Central Apennines, Italy): record of a dominantly pre-orogenic fluid migration. *Solid Earth*, 10: 1355-1383.
- Müller I.A., Fernandez A., Radke J., van Dijk J., Bowen D., Schwiteters J. and Bernasconi, S.M., 2017. Carbonate clumped isotope analyses with the long-integration dual-inlet (LIDI) workflow: scratching at the lower sample weight boundaries. *Rapid Comm. Mass Spectr.*, 2: 1057-1066.
- Müller I.A., Rodriguez-Blanco J.D., Storck J.-C., do Nascimento G.S., Bontognali T.R.R., Vasconcelos C., Benning L.G. and Bernasconi S.M., 2019. Calibration of the oxygen and clumped isotope thermometers for (proto-)dolomite based on synthetic and natural carbonates. *Chem. Geol.*, 525: 1-17.
- Mutti E., Papani L., Di Biase D., Davoli G., Mora S., Segadelli S. and Tinterri R., 1995. Il Bacino Terziario Epimesoalpino e le sue implicazioni sui rapporti tra Alpi ed Appennino. *Mem. Soc. Geol. It.*, 47: 217-244.
- Nesbitt B.E. and Prochaska W., 1998. Solute chemistry of inclusion fluids from sparry dolomites and magnesites in Middle Cambrian carbonate rocks of the southern Canadian Rocky Mountains. *Can. J. Earth Sci.*, 35: 546-555.
- O'Neil J.R., Clayton R.N. and Mayeda T.K., 1969. Oxygen isotope fractionation in divalent metal carbonates. *J. Chem. Phys.*, 51: 5547-5558.
- Parkes R.J., Cragg B.A. and Wellsbury P., 2000. Recent studies on bacterial populations in subsurface sediments: A review. *J. Hydrogeol.*, 8: 11-28.
- Parrish R.R., Parrish C.M. and Lasalle S., 2018. Vein calcite dating reveals Pyrenean orogen as cause of Paleogene deformation in southern England. *J. Geol. Soc.*, 175: 425-442.
- Piana F., Battaglia S., Bertok C., d'Atri A., Ellero A., Leoni L., Martire L. and Perotti E., 2014. Illite (KI) and chlorite (AI) "crystallinity" indices as a constraint for the evolution of the External Briançonnais Front in Western Ligurian Alps (NW Italy). *It. J. Geosci.*, 133 (3): 445-454.
- Piana F., Musso A., Bertok C., d'Atri A., Martire L., Perotti E., Varone D. and Martinotti G., 2009. New data on post-Eocene tectonic evolution of the External Ligurian Briançonnais (Western Ligurian Alps). *It. J. Geosci.*, 128: 353-366.
- Pouchou J.L. and Pichoir F., 1988. Determination of mass absorption coefficients for soft X-rays by use of the electron microprobe. In: D.E. Newbury (Ed.), *Microbeam analysis*. San Francisco Press, San Francisco, p. 319-324.
- Primmer T.J. and Shaw H., 1991. Variations in the δD and $\delta^{18}\text{O}$ compositions of illite-smectites in a partly overpressured Tertiary sequence from an offshore well, Texas Gulf Coast, USA. *Mar. Petrol. Geol.*, 8 (2): 225-231.
- Rankenburg K., Lassiter J.C. and Brey G., 2004. Origin of megacrysts in volcanic rocks of the Cameroon volcanic chain - constraints on magma genesis and crustal contamination. *Contrib. Miner. Petrol.*, 147: 129-144.
- Riding R., 2000. Microbial carbonates: the geological record of calcified bacterial-algal mats and biofilms. *Sedimentology*, 47 (suppl. 1): 179-214.

- Roberts N.M.W. and Walker R.J., 2016. U-Pb geochronology of calcite-mineralized faults: Absolute timing of rift-related fault events on the northeast Atlantic margin. *Geology*, 44 (7): 531-534.
- Roberts N.M.W., Rasbury E., Troy P., Randall R., Smith C.J., Horstwood M.S.A. and Condon D.J., 2017. A calcite reference material for LA-ICP-MS U-Pb geochronology. *Geochem. Geophys. Geosyst.*, 18 (7): 2807-2814.
- Rosenbaum G. and Lister G.S., 2005. The Western Alps from the Jurassic to Oligocene: spatio-temporal constraints and evolutionary reconstructions. *Earth Sci. Rev.*, 69 (3-4): 281-306.
- Rushdi A.I. and Simoneit B.R.T., 2002a. Hydrothermal alteration of organic matter in sediments of the Northeastern Pacific Ocean: Part 1. Middle Valley, Juan de Fuca Ridge. *Appl. Geochem.*, 17: 1467-1494.
- Rushdi A.I. and Simoneit B.R.T., 2002b. Hydrothermal alteration of organic matter in sediments of the Northeastern Pacific Ocean: Part 2. Escanaba Trough, Gorda Ridge. *Appl. Geochem.*, 17: 1401-1428.
- Salih N., Mansurbeg H., Kolo K., Gerdes A., Pr eat A., 2019. In situ U-Pb dating of hydrothermal diagenesis in tectonically controlled fracturing in the Upper Cretaceous Bekhme Formation, Kurdistan Region-Iraq. *Int. Geol. Rev.*, 62: 2261-2279.
- Salomon E., Rotevatn A., Kristensen T.B., Grundv ag S.-A., Hestra G.A., Meckler A.N., Albert R. and Gerdes A., 2020. Fault-controlled fluid circulation and diagenesis along basin-bounding fault systems in rifts - insights from the East Greenland rift system. *Solid Earth*, 11: 1987-2013.
- Shah M.M., Nader F.H., Garcia D., Swennen R. and Ellam R., 2012. Hydrothermal dolomites in the Early Albian (Cretaceous) platform carbonates (NW Spain): nature and origin of dolomites and dolomitizing fluids. *Oil Gas Sci. Technol.*, 67: 97-122.
- Shelton K.I., Hendry J.P., Gregg J.M., Truesdale J.P. and Somerville I.D., 2019. Fluid circulation and fault- and fracture-related diagenesis in Mississippian synrift carbonate rocks on the northeast margin of the metalliferous Dublin Basin, Ireland. *J. Sedim. Res.*, 89: 508-536.
- Simoneit B.R.T. and Lonsdale P.F., 1982. Hydrothermal petroleum in mineralized mounds in the seabed of Guaymas Basin. *Nature*, 295: 198-202.
- Sinclair H.D., 1997. Tectonostratigraphic model for underfilled peripheral foreland basins: An Alpine perspective. *GSA Bull.*, 109 (3): 324-344.
- Stampfli G.M., 1993. Le Brian onnais, terrain exotique dans les Alpes? *Ecl. Geol. Helv.*, 86 (1): 1-45.
- Stampfli G.M. and Borel G.D., 2002. A plate tectonic model for the Paleozoic and Mesozoic constrained by dynamic plate boundaries and restored synthetic oceanic isochrons. *Earth Planet. Sci. Lett.*, 196 (1-2): 17-33.
- Stampfli G.M. and Marthaler M., 1990. Divergent and convergent margins in the north-western Alps - Confrontation and actualistic models. *Geodyn. Acta*, 4: 159-184.
- Stampfli G.M., Borel G.D., Marchant R. and Mosar J., 2002. Western Alps geological constraints on western Tethyan reconstructions. In: G. Rosenbaum and G.S. Lister (Eds.), *Reconstruction of the evolution of the Alpine-Himalayan Orogen*. *J. Virt. Expl.*, 7: 75-104.
- Stolper D.A. and Eiler J.M., 2015. The kinetics of solid-state isotope-exchange reactions for clumped isotopes. A study of inorganic calcites and apatites from natural and experimental samples. *Am. J. Sci.*, 315: 363-411.
- Swennen R., Dewit J., Fierens E., Muechez P., Shah M., Nader F. and Hunt D., 2012. Multiple dolomitization events along the Pozalagua Fault (Pozalagua Quarry, Basque-Cantabrian Basin, Northern Spain). *Sedimentology*, 59: 1345-1374.
- Tavani S., Bertok C., Granado P., Piana F., Salas R., Vigna B. and Mu oz J.A., 2018. The Iberia-Eurasia plate boundary east of the Pyrenees. *Earth Sci. Rev.*, 187: 314-337.
- Taylor H.P.J., 1974. The application of oxygen and hydrogen isotope studies to problems of hydrothermal alteration and ore deposition. *Econ. Geol.* 69: 843-883.
- Vandeginste V., Swennen R., Gleeson S.A., Ellam R.M., Osadetz K. and Roure F., 2005. Zebra dolomitization as a result of focused fluid flow in the Rocky Mountains Fold and Thrust Belt, Canada. *Sedimentology*, 52: 1067-1095.
- Varrone D. and Clari P., 2003. Stratigraphic and paleoenvironmental evolution of the *Microcodium* Formation and the Nummulitic Limestones in the French-Italian Maritimes Alps. *Geobios*, 36: 775-786.
- Wilkinson J.J., 2003. On diagenesis, dolomitisation and mineralisation in the Irish Zn-Pb orefield. *Min. Dep.*, 38: 968-983.
- Woodhead J. and Petrus J., 2019. Exploring the advantages and limitations of in situ U-Pb carbonate geochronology using speleothems. *Geochron.*, 1: 69-84.
- Yang W., Spencer R.J. and Krouse H.R., 1995. Stable isotope and major element compositions of fluid inclusions in Devonian and Cambrian dolomite cements, western Canada. *Geochim. Cosmochim. Acta*, 59 (15): 3159-3172.

Received, February 22, 2021

Accepted, May 7, 2021

First published online, May 30, 2021

